Harnessing ultrasound-derived hydroxyl radicals for the selective oxidation of aldehyde functions

Ari Fischer, Teseer Bahry, Zhangyue Xie, Kaicheng Qian, Renhong Li, James Kwan, François Jerome, Sabine Valange, Wen Liu, Prince Nana Amaniampong, et al.

▶ To cite this version:

Ari Fischer, Teseer Bahry, Zhangyue Xie, Kaicheng Qian, Renhong Li, et al.. Harnessing ultrasound-derived hydroxyl radicals for the selective oxidation of aldehyde functions. ChemSusChem, 2024, 17 (24), pp.e202400838. ⟨10.1002/cssc.202400838⟩. ⟨hal-04785417⟩

HAL Id: hal-04785417

https://hal.science/hal-04785417v1

Submitted on 15 Nov 2024

Harnessing ultrasound-derived hydroxyl radicals for the selective oxidation of aldehyde functions

Ari F. Fischer[†,‡], Teseer Bahry[¶], Zhangyue Xie[†], Kaicheng Qian[§], Renhong Li[§], James Kwan[‖], François Jerome[¶], Sabine Valange[¶], Wen Liu [†,‡]*, Prince N. Amaniampong[¶]* and Tej S. Choksi[†,‡]*

†School of Chemistry, Chemical Engineering and Biotechnology, 62 Nanyang Drive, Nanyang Technological University, 637459, Singapore, Singapore.

‡Cambridge Centre for Advanced Research and Education in Singapore (CARES), 1 Create Way, 138602, Singapore, Singapore.

¶CNRS, Université de Poitiers, Institut de Chimie des Milieux et Matériaux de Poitiers, 1 rue Marcel Doré, Bat B1 (ENSI-Poitiers), 86073 Poitiers, Cedex 9, France

§National Engineering Lab for Textile Fiber Materials and Processing Technology, Zhejiang Sci-Tech University, Hangzhou, 310018, China

‖Department of Engineering Science, University of Oxford, Parks Road, Oxford OX1 3PJ, United Kingdom

*corresponding authors: wenliu@ntu.edu.sg, prince.nana.amaniampong@univ-poitiers.fr, and tej.choksi@ntu.edu.sg

TABLE OF CONTENTS GRAPHIC

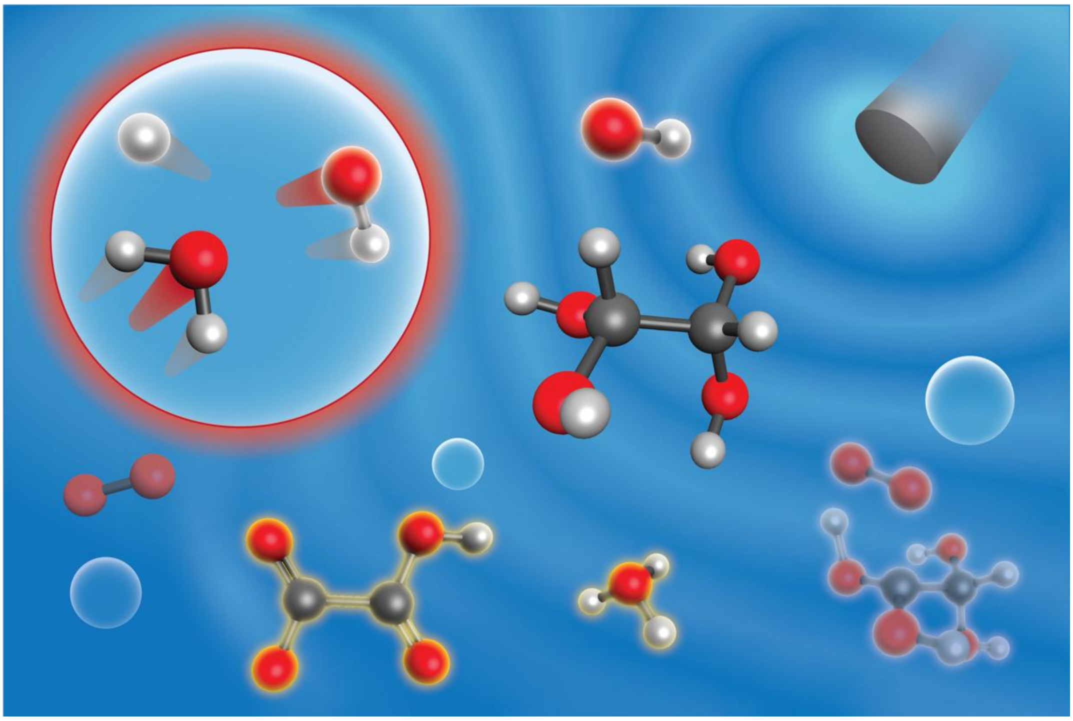

Ultrasound waves emanate from an ultrasound-generating probe. These waves induce the cavitation of gas bubbles driving H_2O dissociation to form hydroxyl radicals. Hydroxyl radicals are transported into aqueous solution where they abstract H-atoms from hydrated glyoxal to initiate oxidation. The selectivity of oxidation products is controlled by the pH of solution and rate of hydroxyl radical formation. Free radicals are shown with a silver glow and ions with a yellow glow.

ABSTRACT

Ultrasonic irradiation holds potential for the selective oxidation of non-volatile organic substrates in the aqueous phase by harnessing hydroxyl radicals as chemical initiators. Here, a mechanistic description of hydroxyl radical-initiated glyoxal oxidation is constructed by gleaning insights from photolysis and radiation chemistry to explain the yields and kinetic trends for oxidation products. The mechanistic description and kinetic measurements reported herein reveal that increasing the formation rate of hydroxyl radicals by changing the ultrasound frequency increases both the rates of glyoxal consumption and the selectivity towards C_2 acid products over those from C-C cleavage. Glyoxal

consumption also occurs more rapidly and with greater selectivity towards C_2 acids under acidic conditions, which favor the protonation of carboxylate intermediates into their less reactive acidic forms. Leveraging such pH and frequency effects is crucial to mitigating product degradation by secondary reactions with hydroxyl radicals and oxidation products (specifically hydrogen peroxide and superoxide). These findings demonstrate the potential of ultrasound as a driver for the selective oxidation of aldehyde functions to carboxylic acids, offering a sustainable route for valorizing biomass-derived platform molecules.

KEYWORDS

Biorefinery, density functional theory (DFT), green chemistry, kinetics, oxidation, sonochemistry.

1. INTRODUCTION

The selective oxidation of aldehyde functions to carboxylic acid groups offers a promising approach for converting biomass-derived compounds into valuable commodity chemicals or chemical intermediates. Examples include converting glucose to gluconic acid[1], glucose-derived isobutaldehyde[2] into isobutyric acid, and glycerol-derived 3-hydroxy-propionaldehyde[3] to 3-hydroxypropionic acid[4]. Such oxidations are ideally performed in aqueous phase to reduce the energetic costs associated with separating these biomass-derived chemicals from the effluents of aqueous hydrolysis[5] or bio-reactors[6].

Aqueous-phase aldehyde oxidation can occur through hydroxyl radical (•OH)-mediated routes ubiquitous in atmospheric chemistry (e.g., glyoxal[7–9], methyl glyoxal[10–12], glycolaldehyde[13]). Generating these •OH initiators is commonly achieved through hydrogen peroxide (H_2O_2) dissociation with ultraviolet radiation or Fenton chemistry[14]. Controlling the selectivity of aldehyde oxidation in the presence of H_2O_2 is difficult, however, due to deleterious H_2O_2-mediated degradation of acid products[15,16]. Hydrogen transfer reactions between H_2O_2 and •OH also scavenge •OH initiators[17], thereby inhibiting the targeted activation of organic substrates by these •OH initiators.

Ultrasound irradiation generates •OH from H_2O homolysis[18] without the need for sacrificial H_2O_2. The H_2O homolysis occurs during the process of inertial cavitation, which involves the quasi-adiabatic compression (>100 bar[19]) and heating (>10^3 K[20–22]) of suspended gas cavities over nanosecond durations[23]. The •OH formed is then transported into solution[18] where it initiates aqueous radical reaction pathways[24–26]. These chemical and physical effects of ultrasound irradiation have enabled diverse oxidation reactions solvated by water, instead of toxic organic solvents [27,28]. Solutes with low vapor pressures are consumed primarily through these •OH-initiated pathways[24,26,29,30] or through pyrolysis reactions near superheated gas-liquid interfaces[19,25,31]. The interfacial pyrolysis reactions of small organic molecules (e.g., amino acids, glucose, acetate[26]) during cavitation of Ar-filled bubbles have been found to be significant only at solute concentrations

≥ 0.1 M [26]. Adding O_2 into these bubbles facilitates •OH formation at relatively lower temperatures reached during collapse[32],[33] as compared with Ar bubbles, likely making interfacial pyrolysis less prevalent. Ultrasound therefore holds potential for controlled •OH-mediated oxidation chemistry of non-volatile solutes in the presence of O_2 at concentrations of typical bioreactors effluents (0.2-1 M) observed during biomass conversion.[6]

Selective aldehyde oxidation to acid products requires reactor conditions (e.g., temperature, pH, reactant concentrations) that maximize rates of the primary •OH-aldehyde reactions while minimizing secondary reactions of •OH with acid products[7,17,34]. The nature and rates of aqueous radical reactions have been extensively characterized in radiolysis, photolysis, and Fenton chemistry[17] and compiled in databases[35]. Computational methods based on density functional theory (DFT)[36–39] enable accurate predictions of kinetics for aqueous radical-reactions with rate constants within 1 kcal mol^{-1} of experimental measurements[39], enabling the parameterization of coefficients in kinetic models not available from experimental studies[40]. Such robust understanding of elementary radical reactions and methods for parameterizing kinetic models enables the quantitative investigation of kinetic regimes for selective aldehyde chemistry.

Experimental and computational techniques are combined here to elucidate the mechanism of ultrasound-mediated oxidation of glyoxal, a C_2 dialdehyde, to C_2 carboxylic acids. This mechanistic inquiry builds upon extensive studies of aqueous •OH-initiated glyoxal oxidation, conducted to address its role in forming aerosols in the atmosphere[8–11,41]. Glyoxal is non-volatile because it readily hydrates to geminal diols in aqueous solution[42]; it therefore does not enter cavitation bubbles, thereby restricting its reactions within the aqueous phase. These characteristics of glyoxal make it an ideal model reactant for understanding sonochemical oxidation of aqueous aldehydes.

First, aqueous •OH are established as the primary drivers of sonochemical glyoxal oxidation (at 5 mM) through kinetic measurements at two ultrasonic frequencies (20 kHz and 580 kHz), electron paramagnetic resonance measurements, and •OH titrations (via H_2O_2[43,44]). These frequencies contrast regimes where mechanical effects (e.g., micro-jetting, mass-transfer, shock waves; 20 kHz) or chemical effects (i.e., radical generation; 580 kHz) of ultrasound are more prevalent[45]. The dilute concentrations facilitate both a mechanistic comparison with atmospheric chemistry and an investigation of sonochemistry under the control of radical pathways. A sonochemical reactor model of •OH-initiated glyoxal oxidation accurately predicts absolute yields and kinetic trends of aqueous products (formic, glyoxylic, and oxalic acids). Yields are predicted with small mean percentage errors at both frequencies (9.8% and 13% at 20 kHz and 580 kHz, respectively) across their ten-fold difference in the rates of •OH supply and of glyoxal consumption.

The analysis of model-predicted product yields reveals that faster •OH formation promotes glyoxal activation and C_2 acid formation in favor of deleterious C-C cleavage. Glyoxal oxidation products (glyoxylate and hydrogen oxalate) is also found to inhibit glyoxal oxidation through competitive reactions with •OH initiators; reactions performed under acidic conditions avoid such inhibition by protonating carboxylate products into carboxylic acids, which react with •OH less rapidly at the carboxy/carboxylate groups and at the α C-H position. These mechanistic insights are leveraged to predict pH values that enable glyoxal oxidation to C_2 acid products at 90-97% yields relative to glyoxal reactants. In doing so, we demonstrate a pathway for the selective oxidation of biomass-derived aldehyde platform molecules into valuable carboxylic acids.

2. RESULTS AND DISCUSSION

2.1. •OH drives ultrasound-mediated aqueous glyoxal oxidation.

Ultrasound was used to generate •OH in aqueous solutions through inertial cavitation in the presence of bubbling O_2. These ultrasound waves were generated continuously at either 20 kHz (0.27 W cm^{-3} at 50% amplitude; 315 K) or 580 kHz (0.48 W cm^{-3} at 100% amplitude; 325 K) in glass ultrasound reactors (**Section 4.1.1**). The rates of •OH formation were assessed by titrating H_2O_2 generated from sonicated H_2O (through •OH coupling[43,44]) in the absence of any solutes (**Section 4.1.1**). The concentrations of H_2O_2 formed are shown in **Figure 1**. These concentrations increased linearly with time at both frequencies (2.6×10^{-8} M s^{-1} (20 kHz) and 2.0×10^{-7} M s^{-1} (580 kHz); **Fig. 1**); the linear trends reflect constant rates of H_2O_2 formation from a continuous supply of •OH. The H_2O_2 formation rates were 8-fold faster at 580 kHz than at 20 kHz, moreover, reflecting a faster supply of •OH available to initiate oxidation chemistry. This relatively faster H_2O_2 formation rate at 580 kHz is consistent with previous reports of faster H_2O_2 formation at frequencies that are larger than 20 kHz

(362 kHz[46] and 615 kHz[47]). Such frequency effects plausibly reflect increase in the density of bubbles undergoing cavitation[48].

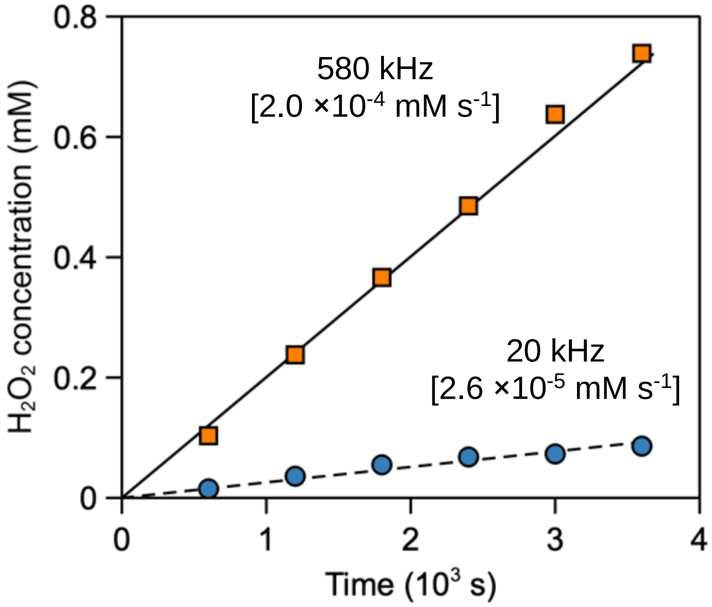

Figure 1: Time-dependent H_2O_2 concentrations during the ultrasonic irradiation of H_2O under 20 kHz (blue ○; 315 K) and 580 kHz (orange □; 325 K) under bubbling O_2 (**Section 4.1.1**). Slopes of linear fits are shown brackets.

Ultrasound irradiation at both frequencies converted aqueous glyoxal (at 5 mM) into organic acids, including oxalic, glyoxylic, glycolic, and formic acids (**Fig. 2a**). Product yields were quantified using high-performance liquid chromatography (HPLC; **Section 4.1.1**). **Figure 2** shows the concentrations of glyoxal and these acid products at different times of exposure to ultrasound at 20 kHz (**Fig. 2b**) and 580 kHz (**Fig. 2c**). These acid products (except glycolic acid) resemble those reported from aqueous •OH-driven glyoxal oxidation reactions,[7–9] where •OH is derived from UV-induced H_2O_2 dissociation. Glyoxal concentrations decreased monotonically with time, reaching fractional conversions of 0.2 after 2.9 ×10^4 s at 20 kHz (**Fig. 2b**) and nearly 1 within 2.2 ×10^4 s at 580 kHz (**Fig. 2c**). These trends show a nearly 10-fold increase in the rate of glyoxal consumption at 580 kHz (3.4 ×10^{-7} M s^{-1}; within 4 ×10^3 s; **Fig. 2c**) compared with 20 kHz (3.5 ×10^{-8} M s^{-1}; averaged over 2.9 ×10^4 s; **Fig. 2b).** These glyoxal consumption rates at each frequency were similar to the •OH formation rates (denoted as $\dot{n}_{OH}$; twice the H_2O_2 formation rates **Fig. 1**) at the same frequency (5.2×10^{-8} M s^{-1} at 20 kHz and 4.0×10^{-7} M s^{-1} 580 kHz). This similarity between •OH formation rates and initial rates of glyoxal consumption indicates that •OH is formed by cavitation at rates that are sufficient to drive the stoichiometric consumption of glyoxal at both frequencies, despite the 8-fold increase in •OH formation rate (**Fig. 1**) and 10-fold increase in glyoxal consumption rate at 580 kHz relative to 20 kHz. Such similar rates, along with the formation of products of a similar nature to H_2O_2/UV-driven glyoxal oxidation, implicates •OH driven radical-mediated reactions as the predominant drivers of ultrasonic glyoxal oxidation.

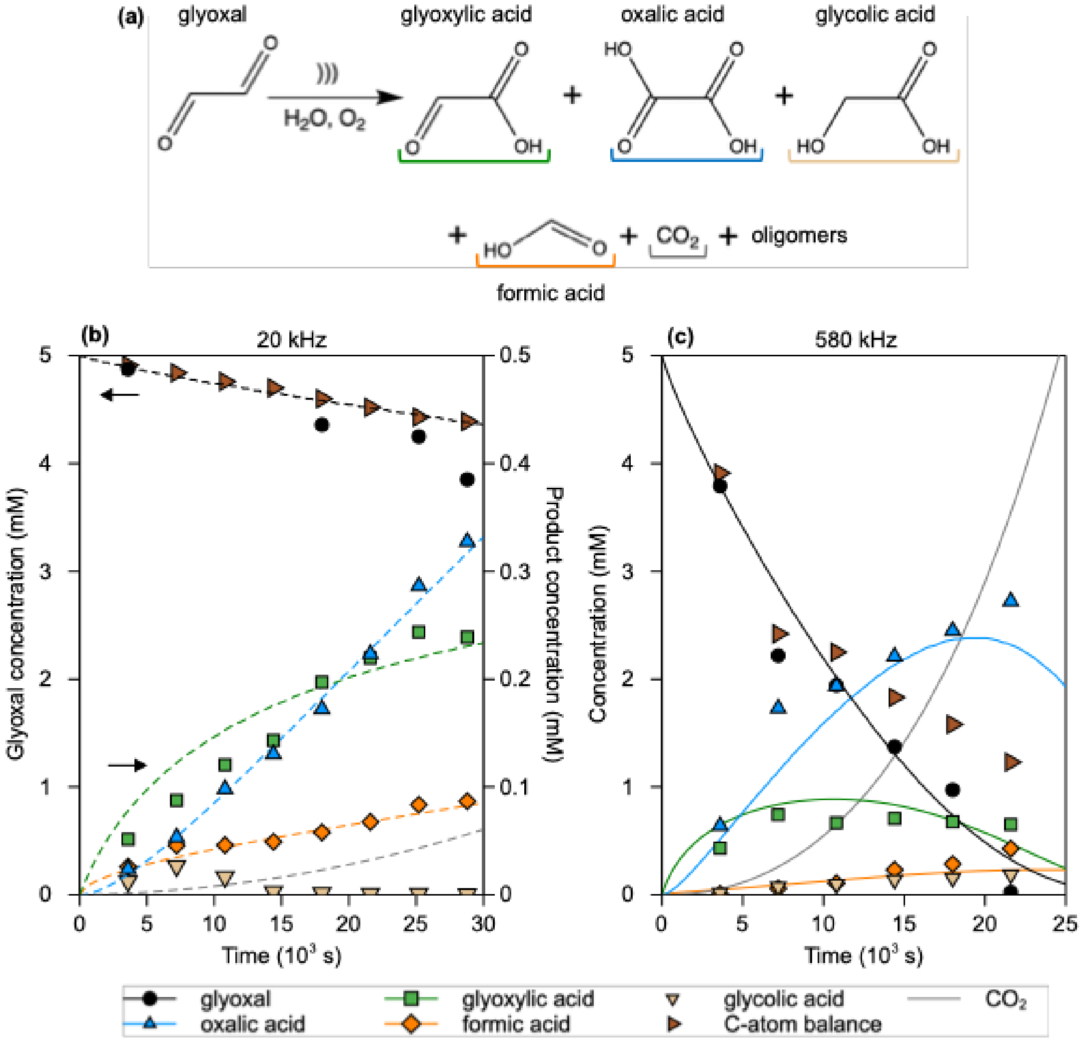

Figure 2: (a) Aqueous glyoxal oxidation under ultrasound irradiation yielding glyoxylic acid (□), formic acid (◇), oxalic acid (△), glycolic acid (▽), and CO_2. (b, c) Time-dependent concentrations of glyoxal (○) and oxidation products during ultrasound irradiation at 20 kHz (b) and 580 kHz (c) under

flowing O_2 (0.33 cm^3 s^{-1}; **Section 4.1.1**). The amount of glyoxal remaining after accounting for C-atoms in measured products (i.e., C-atom balance; ▷; brown) is also shown (b, c). The curves (dashed-20 kHz, solid-580 kHz) represent trends predicted by the mechanism-based kinetic model (**Section 4.2.1**) denoted with the same colors used to depict experimental data. The yield of CO_2, predicted from the model but not measured, is shown in grey. The oligomers are proposed to form through pathways shown in **Section S6**.

The susceptibility of glyoxal to attack by ultrasound-derived •OH was assessed from the electron paramagnetic resonance (EPR) spectra of sonicated aqueous mixtures of 5,5-dimethyl-1-pyrroline N-oxide (DMPO) and glyoxal (50 mM DMPO; 5-50 mM glyoxal; 0.33 cm^3 s^{-1} O_2; pulsed ultrasound at 20 kHz with 16 W cm^{-3} at 25% amplitude; **Section 4.1.2**). The spectra measured at different glyoxal concentrations are shown in **Figure 3**. The predominant signal observed at each glyoxal concentration was associated with the product from •OH addition to DMPO (denoted as DMPO/OH). These DMPO/OH signals reflect aqueous reactions between DMPO and ultrasound-derived •OH[18]. The signals from DMPO/OH adducts decreased in intensity as glyoxal concentrations increased from 0-50 mM (**Fig. 3**). This decrease is illustrated more clearly in **Figure S1**, which shows the maximum height of DMPO/OH signals at different glyoxal concentrations. Such suppression of DMPO/OH signals with the progressive addition of glyoxal indicates that glyoxal competes with DMPO for a limited supply of ultrasound-derived •OH. These rapid glyoxal-•OH reactions initiate reactions of glyoxal even at low concentrations (5-50 mM). Products of these glyoxal-•OH reactions react further to form the different C_1 and C_2 products observed after ultrasonic glyoxal irradiation (**Fig. 2**).

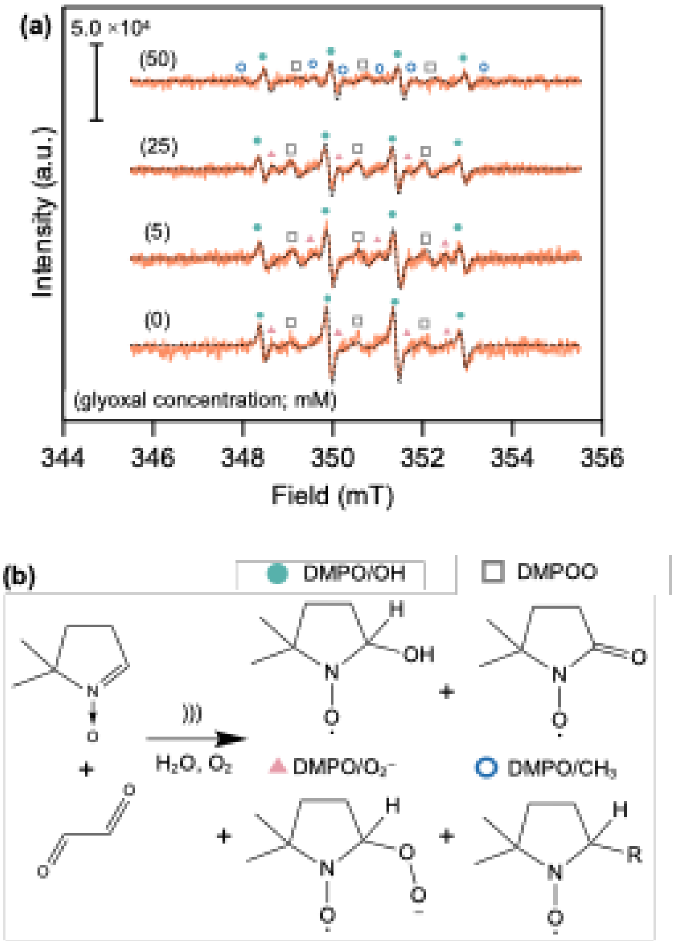

Figure 3: (a) Electron paramagnetic resonance (EPR) spectra for aqueous solutions of 5,5-dimethyl-1-pyrroline N-oxide (DMPO) and glyoxal exposed to pulsed ultrasound at 20 kHz under flow of O_2 (0.33 cm^3 s^{-1}) for 1.2 $\times 10^3$ s (**Section 4.1.2**). The orange solid curves show the measured EPR spectra and the dotted black lines show the fits to combinations of spectra of individual DMPO spin adducts (**Section 4.1.2**). (b) Scheme depicting the formation of different spin adducts formed during DMPO sonication in the presence of glyoxal that correspond to the features measured in (a; identified in **Section S1**).

Glyoxal oxidation by 20 kHz ultrasonic irradiation **(Fig. 2b**) formed oxalic, glyoxylic, and formic acids at concentrations that increased monotonically with ultrasound irradiation time, while glycolic acid was detected at small yields (<0.05 mM) with a maximum value reached within 1 $\times 10^4$ s. Oxalic, glyoxylic, and formic acids were formed at comparable yields below 0.1 mM within 1 $\times 10^4$ s. Glyoxylic and oxalic acids were favored at longer reaction times, however, exceeding yields of 0.2

mM and 0.3 mM, respectively, at 2.9 $\times 10^4$ s while formic acid yields remained below 0.1 mM. A carbon balance revealed that the fraction of the converted C-atoms contained within the quantified products was between 0.53 and 0.76. The C-atoms unaccounted for by these products constitutes, in part, CO_2 and carbonates which could not be quantified with the chromatographic methods used here (**Section 4.1.1**). Oligomers of glyoxal are proposed as additional products needed to close the carbon balance. The structures of these oligomers and the mechanisms for their formation are proposed in **Section S6**.

At the higher frequency of 580 kHz (**Fig. 2c**), concentrations of oxalic, formic, and glycolic acids increased monotonically with ultrasound irradiation time while glyoxylic acid concentrations plateaued below 1 mM. Initial yields to formic acid (within 5 $\times 10^3$ s) were negligible, while yields to oxalic and glyoxylic acids were comparable at 0.5 mM. Oxalic acid was the predominant product formed at later reaction times (after 1.5 $\times 10^4$ s) with concentrations surpassing 2.5 mM. This concentration of oxalic acid represented 50% of the initial glyoxal concentration, and exceeded the concentrations of glyoxylic and formic acid products by five-fold. A balance on C-atoms revealed 0.76-0.93 of the consumed glyoxal was accounted for by these identified acid products. The fraction of glyoxal unaccounted for by these products increased monotonically with increasing glyoxal conversion, exceeding one-tenth of the total amount of glyoxal consumed only after 60% glyoxal conversion (> 1.1 $\times 10^4$ s). Such a large yield of unidentified products only at the later stages of the reaction is consistent with the overoxidation of C_2 acid products to CO_2[7,8].

A comparison of product yields at similar glyoxal conversions of 0.23 (20 kHz, 2.9 $\times 10^4$ s, **Fig. 2b**) and 0.24 (580 kHz, 3.6 $\times 10^3$ s, **Fig. 2c**) under both frequencies underscores the influence of the ultrasound frequency on product selectivity. Yields to glyoxylic and oxalic acids were 1.8 and 2.0 times larger, respectively, under 580 kHz than at 20 kHz. The yield to formic acid under 580 kHz, in contrast, was 9.6 times smaller than that under 20 kHz. These relative yields reveal an enhanced selectivity to C_2 acids in favor of formic acid at the higher glyoxal consumption rates, which was prevalent during ultrasound irradiation at 580 kHz. A robust mechanistic description of these •OH-initiated oxidation reactions is established next in order to understand how the distribution of their products are influenced by changing the ultrasound frequency from 20 kHz to 580 kHz.

2.2. ·OH-initiated glyoxal oxidation mechanisms describe observed kinetic trends.

A sequence of reaction steps was proposed to account for the predominant products (glyoxylic, oxalic, and formic acids and their conjugate bases) formed by sonochemical glyoxal oxidation reactions (**Fig. 4**). Step 1 (**Fig. 4**) shows H_2O homolysis during the inertial cavitation of oxygen bubbles to form •OH and H•. The remaining steps reflect the oxidation of aqueous glyoxal initiated by •OH-glyoxal reactions. The mechanism was adapted from earlier proposals for •OH-initiated glyoxal oxidation[7,8]. Several steps in earlier proposals were omitted here because rate constants calculated using DFT methods indicated that they were too slow to be important. **Section S2** enumerates these omitted reactions and provides a rationale for omitting them. An additional pathway involving $•O_2^-$ (Steps 9-13; **Fig. 4**), not considered previously, was necessary to account for formic acid yields at 20 kHz. Several reaction steps in **Figure 4** group multiple elementary steps together to improve readability, but are expanded in a comprehensive mechanism that is shown in **Figure S2**. These proposed reactions occur alongside the dissociation of glyoxylic acid, oxalic acid, hydrogen oxalate, formic acid, hydrogen peroxide, H_2O, •OOH, and bicarbonate in acid-base equilibrium (**Section S4**).

The mechanism (**Fig. 4**) includes elementary reactions of inorganic radicals (•OH, •OOH, and $•O_2^-$; Steps 2-6). These steps influence the concentrations of the various inorganic radicals in the solution, and in turn dictate the extents of their reactions with organic solutes. Step 2 shows •OH coupling to form H_2O_2. Step 3 shows H-transfer between H_2O_2 and •OH to form •OOH and H_2O. Step 4 shows H-transfer between •OOH and •OH to form O_2 and H_2O. Steps 5 and 6 show reactions between •OOH and either •OOH (5) or $•O_2^-$ (6). Steps 5 and 6 occur via H-transfer (5) or single-electron transfer (6) to form O_2, and either H_2O_2 (5) or HO_2^-(6), respectively. Among these reactions, Steps 2, 4, 5, and 6 terminate radical propagation reactions by coupling unpaired electrons to form molecules in singlet states or O_2 in its triplet ground state.

The mechanism (**Fig. 4**) also includes pathways that oxidize the geminal diol groups of glyoxal.$2H_2O$, glyoxylic acid.H_2O, and glyoxylate.H_2O into glyoxylic acid.H_2O, oxalic acid, and hydrogen oxalate, respectively (Steps 7-8). Here, "$.n\mathrm{H_2O}$" denotes the hydrated form of a species with *n* added H_2O molecules. These hydrates are referred to as *R*-hydroxylmethanol, where "*R"* denotes the dihydroxymethyl (R_a), carboxylic (R_b), and carboxylate (R_c), and the carboxylic acids products are denoted as *R*-formic acids. •OH first abstracts an α-H from a diol group (7) to form *R*-dihydroxylmethyl•. The *R*-dihydroxylmethyl• intermediates further react with O_2 to form *R*-formic acid and •OOH (8) through a two-step addition-elimination (**Fig. S2**).

Steps 9-13 (**Fig. 4**) shows a pathway for formic acid formation from *R*-hydroxylmethanol that is mediated by $•O_2^-$. This pathway was included to reflect the prevalence of $•O_2^-$ formed in acid-base equilibrium with •OOH during the initial stages of the reaction where pH levels are nearly neutral and exceed the pKa of •OOH; 4.48 at 298 K[49]. Step 9 shows the interconversion between the hydrated and aldehyde forms of glyoxal[9], glyoxylic acid, and glyoxylate[50]. The electrophilic nature of the formyl groups in these aldehyde intermediates, denoted as *R*-hydroxyformaldehyde, enables nucleophilic addition by $•O_2^-$, a strong nucleophile[51], to form *R*-methoxide peroxyl• (Step 10). The large pKa values of alkoxide anions with geminal C-OH groups (e.g. hydrated acetaldehyde, 13.5[52]) indicates a significant thermodynamic driving force towards *R*-methoxide peroxyl• protonation to *R*-hydroxymethylperoxyl• (Step 11), the corresponding alcohols. The rapid nature of proton transfer in aqueous solution[53–55] suggests, moreover, that *R*-methoxide peroxyl• protonates rapidly and irreversibly once formed. Step 12 shows O-transfer between the resulting *R*-hydroxymethylperoxyl• and other peroxyl radicals (denoted as R'OO•) to from alkoxyl radicals and O_2. Such peroxyl O-transfer reactions are ubiquitous in autoxidation processes[56] and occur with rapid rate constants. For example, the rate constant for the disproportionation of structurally similar 1-hydroxylethylperoxyl• is 4×10^8 M^{-1} s^{-1} at 298 K[57]. The *R*-hydroxyperoxyl• products from Step 12 undergo rapid β-cleavage (Step 13), also ubiquitous among alkoxyl radicals[56] (> 10^5 s^{-1} calculated with DFT (**Table S2**; 298 K)), to form formic acid and eliminate β-functional groups (*R*) as radicals.

The remaining reactions (Steps 14-22; **Fig. 4**) produce formic acid, formate, and CO_2. Step 14 shows H_2O_2-mediated glyoxylate oxidation to form water, CO_2, and formate[15]. This formate product along with formic acid react further with •OH via alkyl H-transfer to form carboxylate• (R_3; Step 16; **Fig. 4**) and carboxyl• (R_2; Step 18; **Fig. 4**), respectively. Carboxylate• also forms, alongside CO_2 and

OH^-, through an outer-shell electron-transfer reaction between oxalate and •OH (Step 22). Carboxyl• forms from reactions between •OH and oxalic acid (Step 20) and hydrogen oxalate (Step 21) through H and electron transfer, respectively. Carboxylate• reacts with O_2 through single-electron transfer forming CO_2 and $•O_2^-$ (Step 16; **Fig. 4**). Steps 17 and 19 show addition-elimination reactions between O_2 and dihydroxy methyl• and carboxyl•, respectively, to form •OOH and formic acid and CO_2, respectively.

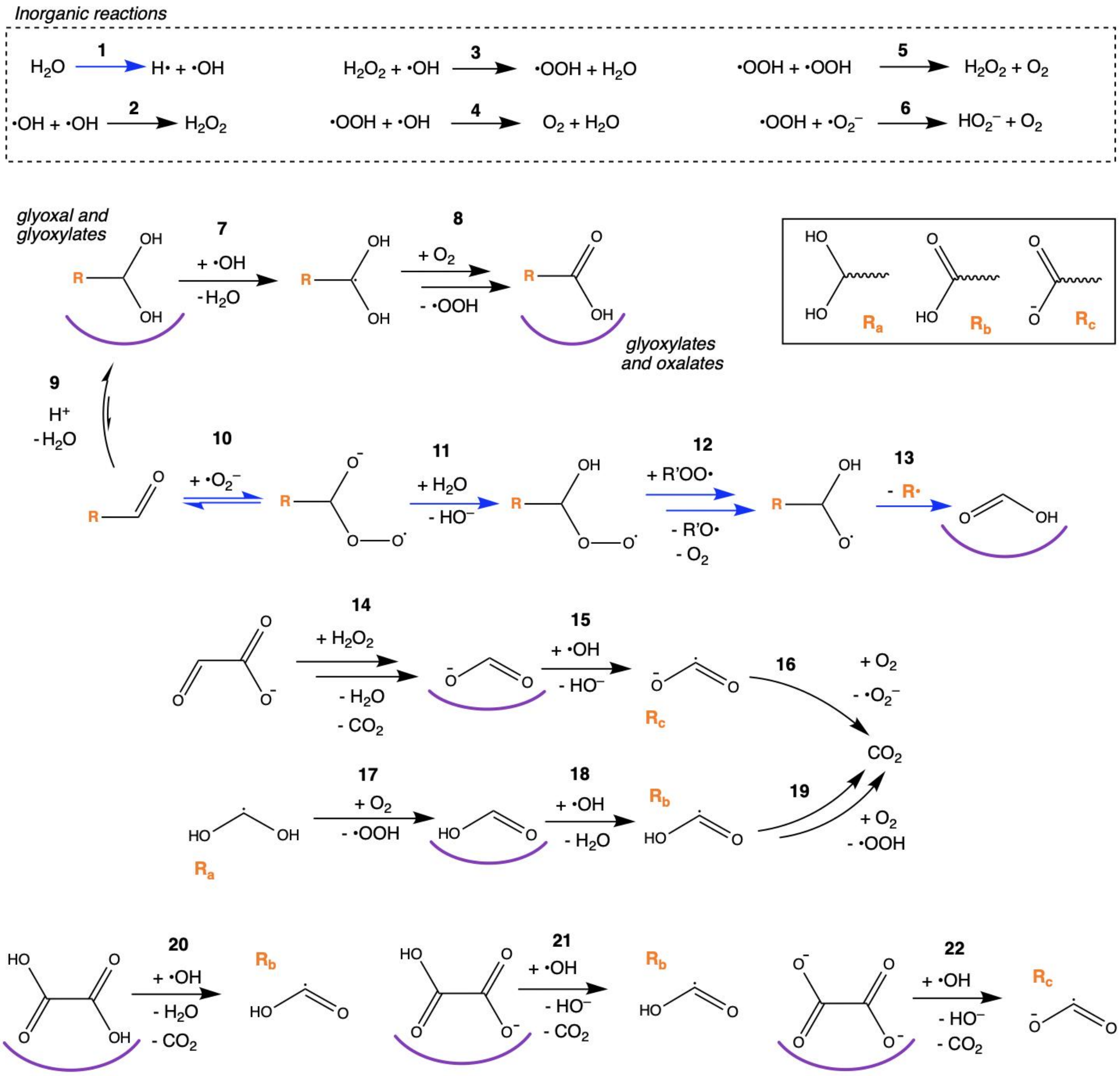

Figure 4: Proposed sequence of steps for aqueous radical-mediated glyoxal oxidation (Steps 2-22) in the presence of O_2. These reactions are initiated by •OH that is derived from ultrasound-induced cavitation events (Step 1). Forward arrows indicate irreversible reactions, forward/backward arrows indicate reversible reactions, and double forward arrows indicate lumped elementary steps that occur

irreversibly. The black arrows denote steps existing in earlier mechanisms[7] and blue arrows denote steps proposed here that were not previously considered. The purple underlines identify the products quantified in experiments (**Fig. 2b,c**).

Time-dependent concentration profiles for reactions under 20 kHz and 580 kHz ultrasound irradiation were predicted using a kinetic model of the reaction steps shown in **Figure S2** to assess contributions of these proposed pathways to sonochemical yields. The model consists of a homogeneous isothermal batch reactor with a constant volume-averaged •OH-formation rate ($\dot{n}_{OH}$) introduced to represent •OH formation from cavitation processes (as described in the **Section 4.2.1**). The values of kinetic and equilibrium coefficients were assigned to those reported from experiments or calculated using theoretical methods (as detailed in the **Section 4.2.2**). These theoretical methods gave free energy barriers that differed from reported experimental values for a set of H-transfer reactions with small mean-absolute errors of 3.6 ± 2.7 kJ mol^{-1}; at 298 K; (**Table S2**). These errors are comparable to definitions of "chemical accuracy"[38,39].

The values of $\dot{n}_{OH}$ and the rate constants for two reaction steps (with forward and reverse rate constants covaried) were regressed to the experimentally measured yields of glyoxylic, oxalic, and formic acid products (**Fig. 2b,c**) at each frequency; their values are reported in **Table 1**. Glyoxal consumption was not included when regressing these parameters because the mass balance was not closed completely (**Fig. 2b,c**) due to the formation of CO_2 and oligomeric species. The regressed rate constants include those for the glyoxal.$2H_2O$-•OH reaction (Step 7a (with "a" denoting the R_a-functionalized reactant); **Fig. 4**; k_{7a}) at both 20 kHz and 580 kHz. In addition, proton transfer from H_2O to 2,2-dihydroxyethoxide peroxyl• (Step 11a; **Fig. 4**; k_{11a}) was regressed at 20 kHz while glyoxylate decomposition by H_2O_2 (Step 14; **Fig. 4**; k_{14}) was regressed at 580 kHz. The rationale for selecting these particular rate constants is provided in **Section 4.2.1** and in **Section S8**. The predicted trends capture the observed glyoxylic, oxalic, and formic acid yields (**Fig. 2b,c**) with small residuals that are within 8.5% and 17% of the mean experimental values at 20 kHz and 580 kHz, respectively (**Table 1**). The ability of the mechanism-based kinetic model to describe observed acid product yields at 20 and 580 kHz with small errors across a wide range of glyoxal conversions supports the proposed origins of these products from the •OH-initiated reaction.

Table 1: Values for average volumetric •OH-formation rates ($\dot{n}_{OH}$) and forward kinetic rate constants for steps in **Figure 4** (k_i), determined by regression (**Section 4.2.2**), experimental benchmarks for these same values, and statistics for the regression. Error ranges denote 95% confidence intervals.

Parameter value	20 kHz		580 kHz	
	Regressed	Benchmark	Regressed	Benchmark
$\dot{n}_{OH}$ (M s^{-1})	3.3 (±0.2) ×10^{-8}	5.2 ×10^{-8} [a]	4.9 (±0.7) ×10^{-7}	4.0 ×10^{-7} [a]
k_{7a} (M^{-1} s^{-1})	3.3 (±0.3) ×10^{8}	8.7 [b]-150 [c] ×10^{7}	1.1 (±0.4) ×10^{9}	1.0-17 [c] ×10^{8}
k_{11a} (M^{-1} s^{-1})	1.2 (±0.3) ×10^{7}	--	--	--
k_{14} (M^{-1} s^{-1})	--	--	2 ±4	16 [d]
Glyoxal consumption rate (M s^{-1}) [e]	2.4 ×10^{-8}	3.5 ×10^{-8}	3.4 ×10^{-7}	3.4 ×10^{-7}
Root-mean-squared error (mM; acid yields)	0.015		0.21	
Mean percentage error				
Acid yields	8.5%		17%	
Glyoxal consumed	30.%		3.7%	

[a] From H_2O_2 titrations (**Fig. 1**). [b] Extrapolated from 298 K[17] with reported E_A[58]. [c] Values reported at reaction temperatures (k_{7a}[58]). [d] From the rate constants reported at 298 K (0.11 M^{-1} s^{-1})[15] referenced to glyoxylate.H_2O, then multiplied by the temperature-dependent equilibrium constant for glyoxylate dehydration[50]. [e] Averaged over the 2.9 ×10^4 s at 20 kHz (**Fig. 2b**) and determined from the first measurement at 580 kHz (4 ×10^3 s; **Fig. 2c**).

The regressed $\dot{n}_{OH}$ values at 20 and 580 kHz differed from their corresponding •OH formation rates measured independently in H_2O_2 titration experiments by factors of 0.63 and 1.2, respectively (**Table 1**). These near-unity values show that ultrasonic irradiation supplies •OH initiators at rates that are similar to amounts that are required to drive glyoxal oxidation reactions through proposed pathways (**Fig. 4**) at both frequencies.

Table 1 compares the regressed values of k_{7a}, and k_{14} to values reported from experimental studies. Regressed k_{7a} values are within the range reported from two different pulse radiolysis studies[17,58] of •OH-glyoxal.$2H_2O$ reactions. The regressed k_{14} value was eight times smaller than the value reported for the H_2O_2-glyoxylate reaction rate measured at 298 K[15]. These comparisons show agreement within an order of magnitude between the regressed rate constants and the experimentally reported benchmarks, thus indicating a reasonable fit.

The regressed k_{11a} value was large (1.2 (±.3) $\times 10^7$; **Table 1**), indicating a rapid rate of proton transfer from H_2O solvent molecules to the oxide group of 2,2-dihydroxyethoxide peroxyl•. Such a large forward rate constant is consistent with the low barriers reported for protonation of alkoxides by alcohols (of order 8 kJ mol^{-1} between methanol and methoxide present as gaseous dimers[54]). The rapid nature of proton transfer between H_2O and ^{-}OH[59][57] suggests, moreover, that H_2O can rapidly donate protons to anionic bases. Such precedence for H_2O and alkoxides as proton donors and acceptors, respectively, suggests that the large regressed value for k_{11a} is reasonable.

The model under-predicted extents of glyoxal consumption at 20 kHz (0.12-1.1 mM; not included in the set of regressed output data), on the other hand, with predicted values that were within 30% of measured values, on average. This underprediction reflects an incomplete balance of C-atoms consumed by glyoxal oxidation to glyoxylic acid, oxalic acid, formic acid, and CO_2 products proposed in **Figure 4**; it is not, moreover, accounted for by the small measured, but not simulated, yields of glycolic acid. This underprediction is nearly commensurate with the 0.63-fold smaller regressed $\dot{n}_{OH}$ value than the $\dot{n}_{OH}$ value determined from H_2O_2 titration (**Table 1**). This comparison suggests that the stoichiometric consumption of glyoxal by the amounts of •OH observed in excess of the stoichiometric requirements for driving reactions in **Figure 4** could nearly close the C-atom balance. We propose that such excess •OH initiates oligomerization through addition-elimination reactions between R-dihydroxylmethyl• and glyoxal.H_2O (**Figures S6** and **S7**). This proposed mechanism is analogous to ketyl radical addition to hydrated methylglyoxal, which was proposed to occur during methylglyoxal oxidation[11]. **Section S6** shows that the thermodynamics for the proposed pathway are favorable (**Table S4**). The small enthalpic barriers for alkyl radical addition to carbonyls[60] and large rate constants for β-cleavage of alkoxyl radicals[56] suggest, moreover, that the proposed pathway is kinetically accessible. This proposed pathway can also account for the formation of products with larger molecular weights that were reported in glyoxal oxidation driven by UV/H_2O_2[7] (**Figure S8**).

The model also predicted extents of glyoxal consumption at 580 kHz (1.2-5.0 mM; not included in the set of regressed output data) that were within 3.7% of measured values. Such alignment demonstrates that the homogeneous reactions responsible for forming predominant acid products account entirely for the glyoxal consumed. Hence, the chemical effects of ultrasound under these conditions arise from the generation of •OH, akin to UV-induced or Fe^{2+}-catalysed H_2O_2 dissociation[14], rather than from competing processes such as pyrolysis of solutes in hot spots near superheated bubbles[19,26]. Consequently, ultrasonic irradiation at 580 kHz presents a viable strategy for driving glyoxal oxidation with chemical origins predominantly from aqueous radical chemistry.

2.3. Increases in rates of •OH formation consume glyoxal faster and with greater selectivity to C_2 acids.

The kinetic model was leveraged to understand the influence of an increase in •OH formation rates at 580 kHz compared with 20 kHz on both the rates of glyoxal consumption and the selectivity to C_2 acids (in favor of formic acid) (**Fig. 2 b,c**). **Figure 5** shows rates of glyoxal consumption through the oxidation pathways in **Figure 4** obtained from the kinetic model at 20 kHz and 580 kHz, plotted against extents of glyoxal consumption through these same pathways (denoted as ϵ). These reaction extents do not include amounts of glyoxal consumed to form oligomers or other products that remained unidentified **Figure 4**. The limits plotted in **Figure 5** were selected to encompass extents achieved within the timescales of experiments. These extents were 0.62 mM at 20 kHz (denoted as ϵ_{LF}; **Fig. 2b**) and 4.7 mM at 580 kHz (denoted as ϵ_{HF}; **Fig. 2c**). The reaction rates are compared with regressed rates of •OH formation ($\dot{n}_{OH}$; **Table 1**) and with the rates of glyoxal activation by •OH in Step 7a (**Fig. 4**).

The rates of glyoxal consumption and of glyoxal-•OH reactions were similar to each other at both frequencies, irrespective of the extent of reaction (**Fig. 5**). Such similar rates indicate that glyoxal is consumed predominantly through stoichiometric reactions with •OH (Step 7a; **Fig. 4**), in favor of its reactions with $•O_2^-$ (Step 10a; **Fig. 4**). These glyoxal-•OH reaction rates consumed between 50-100% of the •OH generated within a reaction extent of ϵ_{LF} at both frequencies. Such selective attack of glyoxal by •OH indicates that changes to rates of •OH formation due to changes in the ultrasound frequency (**Table 1**) drives a nearly commensurate increase in the amount of glyoxal consumed. To illustrate, regressed $\dot{n}_{OH}$ values were 15 times larger at 580 kHz than at 20 kHz (**Table 1**). This increase in $\dot{n}_{OH}$ accounts for the nearly proportional increase in glyoxal consumption rates (by 14-fold) at 580 kHz than at 20 kHz (**Table 1**) obtained from the model. Such proportionality between •OH formation and glyoxal consumption rates underlies the relatively faster rates of glyoxal consumption observed at 580 kHz than at 20 kHz in experiments (**Table 1**).

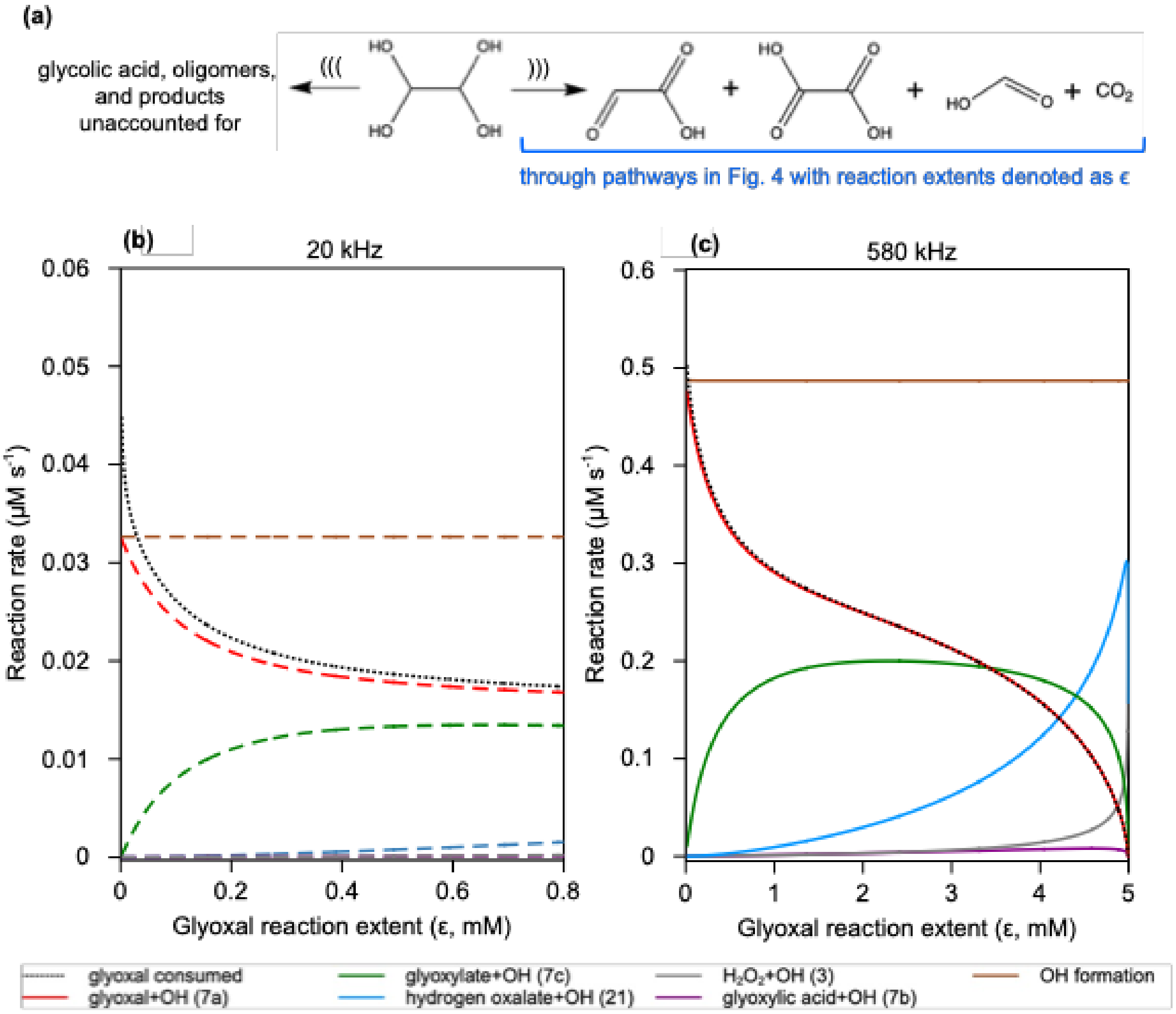

Figure 5: Rates of aqueous glyoxal consumption, •OH formation, and of net rates of reactions involving •OH from the kinetic model (**Section 4.2.1**) at 20 kHz (a) and 580 kHz (b). Rates at 20 kHz and 580 kHz are represented using dashed and solid-lines, respectively. Rates are shown at different extents of glyoxal consumption (ϵ). The legend denotes the corresponding reaction steps in **Figure 4**.

These steps include those with rates that exceed 10% of the •OH formation rate at either frequency (**Section S7**).

The interplay between rates of steps at key branching points in the glyoxal oxidation mechanism (**Fig. 4**) determines the relative yields to the C_2 acids (glyoxylates and oxalates), formates, and CO_2 products formed. Here, formates, glyoxylates, and oxalates refer to carboxylic acids grouped together with their conjugate bases, and including any hydrated forms. **Figure 6** shows a simplified representation of the reactions in **Figure 4** that combines sequences of reaction steps to illustrate the branching points. The C_2 acids form through pathways initiated by glyoxal.$2H_2O$-•OH reactions (Step 1; **Fig. 6**). Formates, on the other hand, form by glyoxylate oxidation by H_2O_2 (Step 7; **Fig. 6**) and through glyoxal.H_2O oxidation by $•O_2^-$ (Step 9; **Fig. 6**). Finally, CO_2 forms through both glyoxylate oxidation by H_2O_2 (Step 7; **Fig. 6**), by •OH-mediated formate oxidation (Step 10; **Fig. 6**), and by secondary reactions of oxalates with •OH (Steps 4-6; **Fig. 6**). These pathways show that yields of C_2 acid products decrease by oxidizing further to form formic acid (Step 7; **Fig. 6**) and CO_2 (Steps 4-7,10; **Fig. 6**).

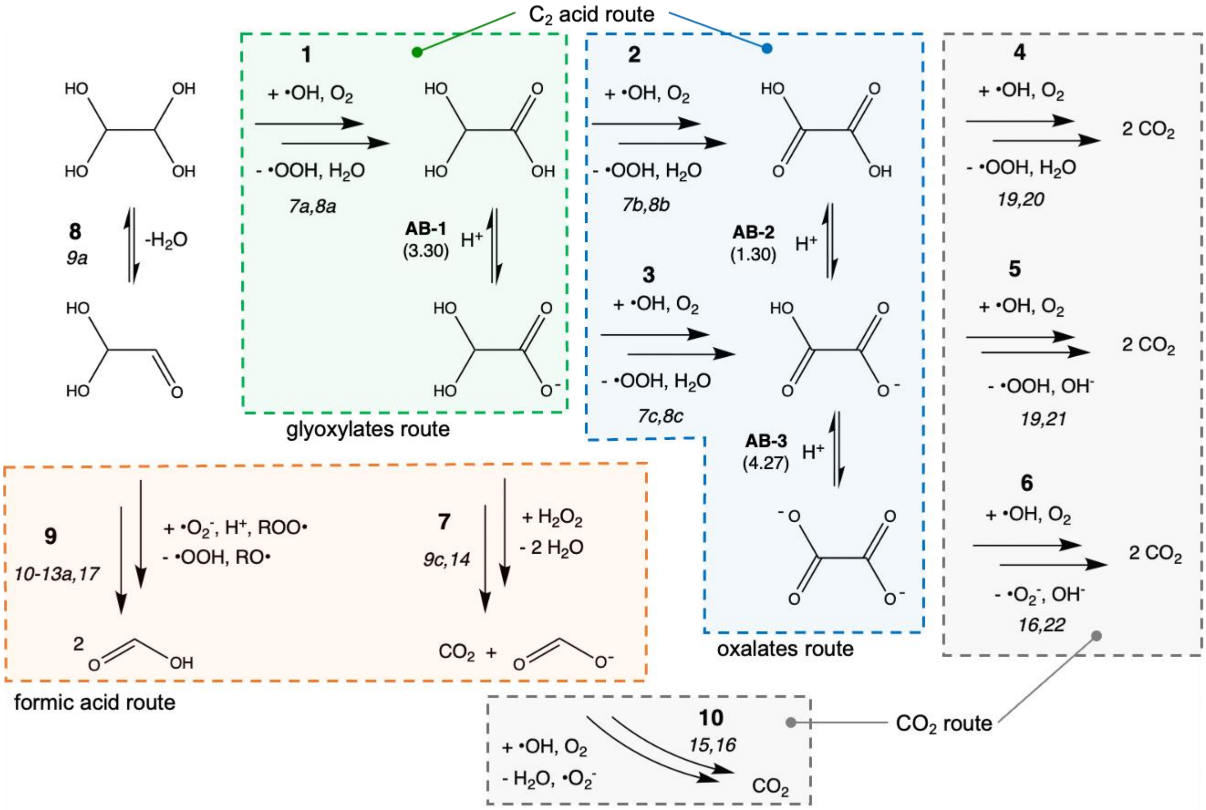

Figure 6: Sequence of reaction steps adapted from **Figure 4** to illustrate key branching points in the mechanism that yield C_2 acids (glyoxylates and oxalates), formates, and CO_2 as products. The forward/backwards arrows denote equilibrated reactions and the double forward arrows indicate lumped elementary steps that occur irreversibly. The italicized numbers denote corresponding steps in **Figure 4**. The **AB-*i*** labels denote acid-base equilibrium reactions and the ***i*** labels denote all other steps. The parenthesis beneath **AB-*i*** indicate the pKa values of the acids at 298 K (**Table S3**).

The ultrasound frequency influences the branching between different routes (**Fig. 6**), at least in part, by changing the rate that •OH initiators are formed ($\dot{n}_{OH}$). To illustrate this effect, **Figure 7** depicts C_2 acid and formates yields from the kinetic model and from experiments (**Fig. 2b,c**) at different ϵ values. Model-predicted formates and C_2 acid yields increased linearly within reaction extents of ϵ_{LF} (0.62 mM) under ultrasound irradiation at both 20 kHz and 580 kHz. These model-predicted C_2 acid yields were on average 1.1 times larger at 580 kHz than at 20 kHz. Conversely, the model-predicted formates yields were on average 2.8 times smaller at 580 kHz than at 20 kHz.

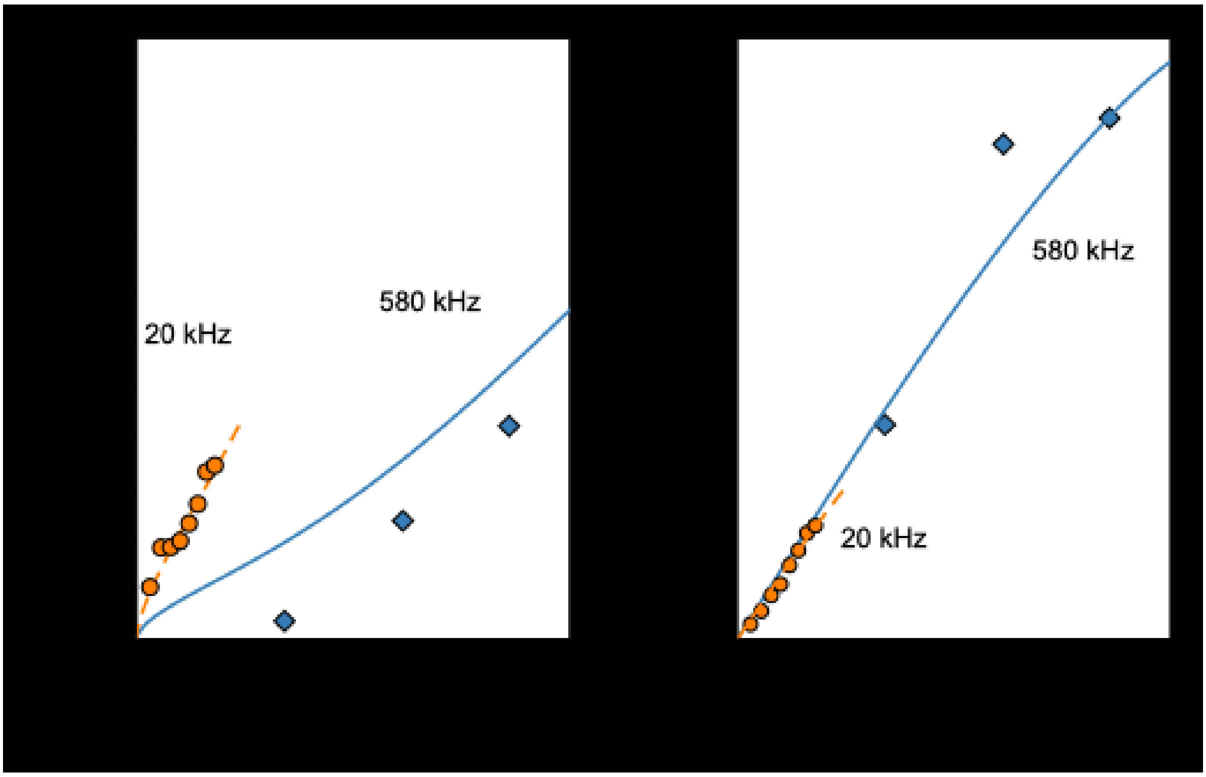

Figure 7: Yields to formates (a) and C_2 acids (glyoxylates and oxalates; b) at different ϵ values at 20 kHz (orange circles and dashed curves) and 580 kHz (blue diamonds and solid curves). Symbols show experimental measurements and curves were calculated using the kinetic model (**Section 4.2.1**) evaluated at 20 kHz (dashed) or 580 kHz (solid).

Figure 7 shows that C_2 acids formed more selectively at 580 kHz than at 20 kHz, even at the same reaction extent ϵ. An expression for the selectivity to C_2 acids, denoted as $S_{C_2,FA}$, is defined by dividing the rate of C_2 acid formation (r_{C_2}) by the rate of formates formation (r_{FA}):

$$S_{C_2,FA} = \frac{r_{C_2}}{r_{FA}} \qquad (1)$$

Figure 8 shows $S_{C_2,FA}$ values obtained from the kinetic model at 20 kHz and 580 kHz at different ϵ values. $S_{C_2,FA}$ values follow a similar shaped curve at both frequencies with a steep initial increase that peaks before 0.6 mM, then decreases. The average $S_{C_2,FA}$ value within an extent of ϵ_{LF} was 3.4 times larger at 580 kHz (25) than at 20 kHz (7.3), consistent with the greater relative yields to C_2 acids in favor of formates at 580 kHz.

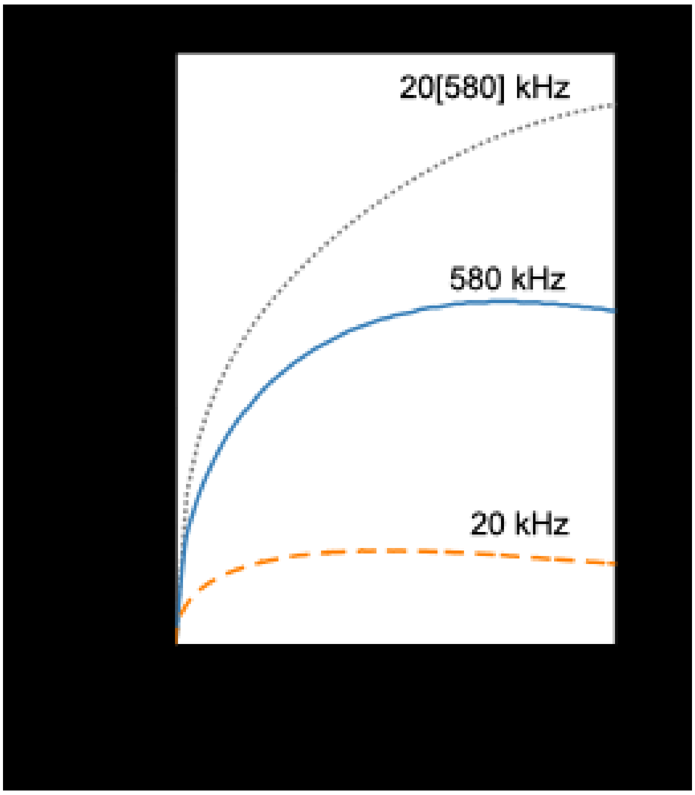

Figure 8: The rate of C_2 acid (glyoxylates and oxalates) formation divided by the rate of formates formation ($S_{C_2,FA}$; **Eq. 1**) at different extents of glyoxal consumption (ϵ). These rate ratios were obtained from the kinetic model (**Section 4.2.1**) evaluated under 20 kHz (orange-dashed) and 580 kHz (blue-solid) of ultrasound irradiation. Trends are also shown for the model evaluated at 20 kHz with the fitted $\dot{n}_{OH}$ value replaced with the fitted value at 580 kHz (denoted as 20[580] kHz; grey-dotted).

Changes to $\dot{n}_{OH}$ values not only influence the rates of glyoxal activation by •OH but also the selectivity to different oxidation products. This is because the concentrations of •OH and glyoxal oxidation products, and the relative rates of reactions that they mediate, adjust to different $\dot{n}_{OH}$ values in order to maintain a balance at steady-state. The influence of $\dot{n}_{OH}$ on $S_{C_2,FA}$ values cannot be assessed directly from comparisons between 20 kHz and 580 kHz, however, because the operating temperatures of the 20 kHz and 580 kHz ultrasound reactors differ by 10 K (**Section 4.1.1**). The influence of $\dot{n}_{OH}$ on $S_{C_2,FA}$ values was investigated instead by simulating glyoxal oxidation at the steady-state temperature of the 20 kHz reactor (315 K) using the regressed parameters from the 20 kHz kinetic model (**Table 1**), but using the $\dot{n}_{OH}$ value from the 580 kHz kinetic model (denoted as $\dot{n}_{OH}$[580 kHz]; **Table 1**). This kinetic model, denoted as "20[580] kHz", simulates the influence of a larger $\dot{n}_{OH}$ value on the kinetics of glyoxal oxidization at 20 kHz, without confounding the influence of temperature. The simulated values of $S_{C_2,FA}$ at 20[580] kHz are shown at different ϵ values in **Figure 8**. The $S_{C_2,FA}$ values increased monotonically with ϵ at 20[580] kHz. This average $S_{C_2,FA}$ value (within an extent of ϵ_{LF}; 35), moreover, was within a factor of 1.4 of the average $S_{C_2,FA}$ value at 580 kHz (25). This average value at 20[580] kHz was 4.7 times larger, on the other hand, than the average $S_{C_2,FA}$ value at 20 kHz (7.3). Such similar $S_{C_2,FA}$ values at 20[580] kHz and at 580 kHz, which both exceed values at 20 kHz, demonstrate that oxidation reactions are more selective to C_2 acids at 580 kHz than at 20 kHz (**Fig. 7**), in large part, because of a larger $\dot{n}_{OH}$ value.

A kinetic analysis based on the degree of rate control formalisms[61,62] (**Section S5**) was performed to uncover how changes to rates of individual reaction steps influence the selectivity to C_2 acids ($S_{C_2,FA}$). This analysis begun by determining approximate expressions for r_{C_2} and r_{FA} (**Section S5**). r_{C_2} was approximately equal to the rate of the glyoxal.2H_2O-•OH reaction (Step 7a; **Fig. 4**). r_{FA} was approximately equal to the sum of the rates of H_2O_2-mediated glyoxylate oxidation (Step 14; **Fig. 4**) and •O_2^--mediated glyoxal.H_2O oxidation (Steps 9a-13a; **Fig. 4**) minus the rate of •OH-mediated formate oxidation. An expression for $S_{C_2,FA}$ restated in terms of these kinetically relevant steps in these pathways ($S^0_{C_2,FA}$) is given in **Equation 2**; its derivation is provided in **Section S5**.

$$S^0_{C_2,FA} = \frac{k_{7a}[\bullet\, OH][gly.2H_2O]}{2k_{11a}K_{10a}[\bullet\, O_2^-][gly.H_2O] + k_{14}[H_2O_2] - -k_{15}[\bullet\, OH][HCOO^-]} \qquad (2)$$

In **Equation 2**, $[\bullet\, OH]$, $[gly.2H_2O]$, $[\bullet\, O_2^-]$, $[gly.H_2O]$, $[H_2O_2]$, $[glyox^-]$, and $[HCOO^-]$ are concentrations of •OH, glyoxal.2H_2O, •O_2^-, glyoxal.H_2O, H_2O_2, glyoxylate.H_2O, and formate, respectively. The $K_{10a}[\bullet\, O_2^-][gly.H_2O]$ product in the denominator of **Equation 2** reflects the concentration of dihydroxyethoxide peroxyl•, which reacts in a kinetically relevant proton-transfer reaction with H_2O (Steps 11a; **Fig. 4**), formed in quasi-equilibrium with •O_2^- and glyoxal.H_2O. This quasi-equilibrium reflects the faster rate of •O_2^- elimination from dihydroxyethoxide peroxyl• than for proton transfer with H_2O, as discussed in **Section S5**. The factor of two before k_{11a} reflects the formation of two stoichiometric equivalents of formates formed for each •O_2^--mediated glyoxal.H_2O oxidation event.

Equation 2 shows that $S^0_{C_2,FA}$ values depend on concentrations of glyoxal reactants (in hydrated or aldehyde forms), of •OH, and of products formed from glyoxal oxidation mechanisms (•O_2^-, H_2O_2, glyoxylate, and formate). The concentrations of these species, obtained from kinetic models of glyoxal oxidation (**Section 4.2.1**), are shown in **Figure 9** at 20 kHz and at 20[580] kHz and with different ϵ values. A comparison between the concentrations of glyoxylate and H_2O_2 at 20 kHz and at 20[580] kHz reveals slightly larger average values (1.1 and 1.1, respectively, within an extent of ϵ_{LF}) with the larger $\dot{n}_{OH}$ value at 20[580] kHz (**Fig. 9a**). Such increases correspond to only a 1.2-fold increase in the driving force for the H_2O_2-glyoxylate reaction (Step 7; **Fig. 6**). The concentration of •O_2^- was 3.6 times larger at 20[580] kHz than at 20 kHz (**Fig. 9b**), indicating a commensurate increase in rates of glyoxal-•O_2^- reactions (Step 9; **Fig. 6**). The •OH concentration, in contrast, was 15-fold larger at 20[580] kHz than at 20 kHz (**Fig. 9b**); this increase results in a commensurate increase in the rates of •OH-mediated glyoxal oxidation (Step 1; **Fig. 6**). The larger •OH concentration also enhances the rates of the •OH-mediated formate oxidation (Step 10; **Fig. 6**); this enhancement is counteracted, however, by a 0.27 times smaller formate concentration at 20[580] kHz than at 20 kHz (**Fig. 9a**). These larger •OH concentrations promote •OH-mediated glyoxal oxidation to C_2 acids (Step 1; **Fig. 6**) to a greater extent than any changes to the rates that formates form (Steps 7,9, and 10; **Fig. 6**). This analysis reveals that the greater concentration of •OH sustained by faster •OH formation promotes the attack of the glyoxal reactant by •OH initiators preferentially over deleterious C-C cleavage reactions involving glyoxal oxidation products.

The 15-fold increase in •OH concentration calculated at 20[580] kHz, compared with 20 kHz, is commensurate with the increase in regressed $\dot{n}_{OH}$ values (15; **Table 1**). Such proportionality reflects the highly reactive nature of •OH which establishes low pseudo-steady state thresholds that balance their rates of formation from cavitation processes and consumption via homogeneous reactions. A comparison between the rates shown in **Figure 5** reveals that stoichiometric reactions of •OH with glyoxal.$2H_2O$ (Step 7a; **Fig. 4**) and glyoxylate.H_2O (Step 7c; **Fig. 4**) consume nearly all of the •OH formed (>95%) within a reaction extent of ϵ_{LF}. Pseudo-steady state •OH concentrations can therefore be expressed by equating •OH formation rates ($\dot{n}_{OH}$) with rates of reactions with glyoxal and glyoxylate hydrate, and isolating $[\bullet\ OH]$ from the resulting relation:

$$[\bullet\ OH] = \frac{\dot{n}_{OH}}{k_{7a}[gly.2H_2O] + k_{7c}[glyox^{-}.H_2O]} \tag{3}$$

Here, $[glyox^{-}.H_2O]$ is the concentration of glyoxylate hydrate and k_{7c} is the rate constant for Step 7c (**Fig. 4**). The form of **Equation 3** shows an increase in •OH concentration in proportion to $\dot{n}_{OH}$, and an inverse dependence on $[gly.2H_2O]$ and $[glyox^{-}.H_2O]$. The denominator of **Equation 3** is nearly unchanged as the $\dot{n}_{OH}$ value increases in the 20[580] kHz model from the value in the 20 kHz, when comparing reactions at the same conversion (and the same $[gly.2H_2O]$ values, in turn). This is because $[glyox^{-}.H_2O]$ concentrations are nearly unaffected by the change in $\dot{n}_{OH}$, as evident from the $[glyox^{-}]$ concentrations in **Figure 9a**. Such a constant denominator accounts for the proportionality between calculated $[\bullet\ OH]$ and regressed $\dot{n}_{OH}$ values. This proportionality underscores that increasing $\dot{n}_{OH}$ at a higher ultrasound frequency of 580 kHz not only accelerates reactions by providing initiators faster, but also enhances rates of reaction steps that involve •OH as a stoichiometric reactant due to elevated •OH concentrations. The twin effects of increasing $\dot{n}_{OH}$ and $[\bullet\ OH]$, as the ultrasound frequency increases from 20 kHz to 580 kHz, explains, in part, the increase in the selectivity to C_2 carboxylic acids relative to formates at higher frequencies.

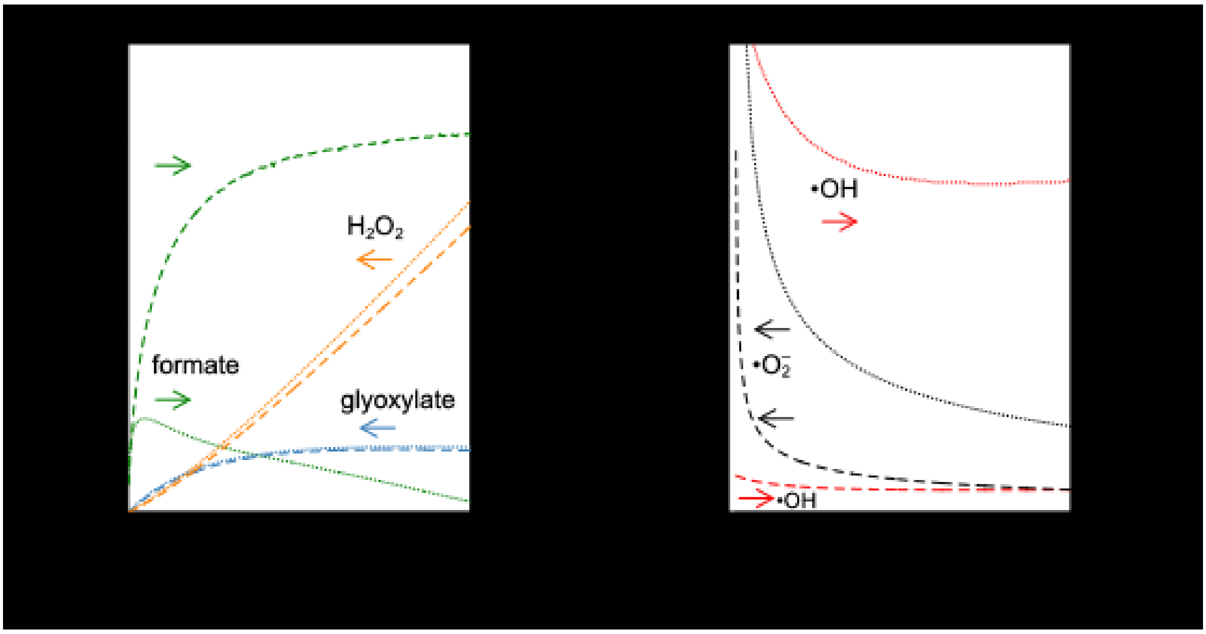

Figure 9: Predicted concentrations of reactive intermediates in glyoxal oxidation reactions including H_2O_2 (orange, a), glyoxylate (aldehyde form; blue, a), formate (green, a), $•O_2^-$ (black, b), •OH (red, b) at 20 kHz (dashed) and 20[580] kHz (dotted; **Fig. 8**) with different extents of glyoxal consumption (ϵ).

2.4. Glyoxal oxidation forms C_2 acid products more selectively under acidic conditions by avoiding reactions of •OH with carboxylates.

Initial rates of glyoxal consumption at both 20 kHz and 580 kHz calculated using kinetic models (**Section 4.2.1**) mirrored the respective rates of •OH formation (**Fig. 5**). Given the one-to-one stoichiometry of glyoxal.$2H_2O$ activation by •OH (Step 7a; **Fig. 4**), the similar initial rates of glyoxal consumption and •OH formation indicates that •OH was captured completely by glyoxal. Rates of glyoxal consumption decreased at higher conversions (**Fig. 5**), despite constant rates of •OH formation, reflecting significant rates of •OH reactions with other substrates in competition with glyoxal. Specifically, a comparison between rates of •OH consumption through different reaction steps (**Fig. 4**) revealed significant rates (i.e., >10% of the •OH formation rate; **Fig. S9**) not only through reactions with glyoxal.$2H_2O$ (Step 7a; **Fig. 4**), but also through glyoxylate.H_2O (Step 7c; **Fig. 4**), H_2O_2 (Step 3; **Fig. 4**), and hydrogen oxalate (Step 21; **Fig. 4**). The rates of these kinetically relevant steps for •OH-consumption at different extents of glyoxal consumption (ϵ; **Fig. 5**) are shown **Figure 5** at 20 kHz and 580 kHz.

The rates of the glyoxylate.H_2O-•OH reaction (Step 7c; **Fig. 4**) at both frequencies increased rapidly at low ϵ values (<0.5 mM; **Fig. 5**) before reaching a plateau. Rates decreased precipitously at higher ϵ values (>4 mM) accessed at 580 kHz. The rates of •OH reactions with hydrogen oxalate (Step 21; **Fig. 4**) and H_2O_2 (Step 3; **Fig. 4**), on the other hand, increased monotonically with conversion following concave up trends at both frequencies. These kinetic trends show that at higher ϵ, glyoxal reacts with •OH at slower rates as glyoxylate.H_2O, hydrogen oxalate, and H_2O_2 scavenge •OH.

Bimolecular H-transfer between •OH and glyoxal.$2H_2O$ or glyoxylate.H_2O occurs at rates that are proportional to the concentrations of •OH and the respective H-donor. Glyoxylate.H_2O and glyoxal.$2H_2O$ were consumed at rates (via •OH) within a factor of two of each other (> 0.6 ϵ; **Fig. 5**), even when glyoxylate.H_2O was 16 times less abundant than glyoxal.$2H_2O$ (at 0.6 ϵ; **Fig. S10**). These comparable rates even with such small glyoxylate.H_2O concentrations reflect the relatively larger rate constant for abstracting the alkyl H-atom from glyoxylate.H_2O by •OH than from glyoxal.$2H_2O$. The larger rate constant is evident from values reported experimentally (**Table 1**), regressed to the kinetic data (**Table 1**), and derived from DFT (at 298 K; **Table S2**). This rapid reaction between •OH and glyoxylate.H_2O scavenges •OH that would otherwise activate glyoxal to initiate C_2 acid formation (Step 1; **Fig. 6**). This reaction also rapidly converts glyoxylate.H_2O into hydrogen oxalate (Step 3; **Fig. 6**), thereby limiting glyoxylate.H_2O yields to small fractions of initial glyoxal concentrations.

Glyoxylate.H_2O forms during glyoxal oxidation in acid-base equilibrium with glyoxylic acid.H_2O (Step AB-1; **Fig. 6**). The acid-base equilibrium shifts in favor of glyoxylic acid.H_2O as acid products derived from glyoxal accumulate and the pH drops below the pKa of glyoxylic acid (3.12 at 20 kHz (315 K) and 3.03 at 580 kHz (325 K); **Table S3**) with increasing reaction time. Here, 315 K and 325 K represent the steady state bulk temperature under 20 kHz and 580 kHz of ultrasound irradiation. This pH drop and the corresponding shift in acid-base equilibrium is illustrated in **Fig. S11**, which shows pH values and the fractions of glyoxylates (glyoxylic acid and glyoxylate in aldehyde and hydrated forms) present as glyoxylic acid.H_2O. Furthermore, glyoxylic acid.H_2O reacts less rapidly with •OH than glyoxylate.H_2O does, as indicated by lower rate constants for the former (**Table S2**). This smaller rate constant indicates that the pool of glyoxylates is oxidized (Steps 2,3; **Fig. 6**) less rapidly by •OH under acidic conditions with glyoxylic acid.H_2O present in its neutral form.

The effect of pH on the oxidation of glyoxylates (Steps 2,3; **Fig. 6**) is evident from **Figure S12**, which shows the calculated rate that the pool of glyoxylates reacts with •OH at 20 kHz and 580 kHz (from the kinetic model; **Section 4.2.1**). **Figure S12** also shows a hypothetical rate of reaction if all of the glyoxylates were present as anions. The rates under acid-base equilibrium were 1.4 and 3.9 times smaller, on average, than the hypothetical rates of glyoxylate.H_2O anions at 20 kHz and 580 kHz within reaction extents of ϵ_{LF} and ϵ_{HF}, respectively. The slower rates prevalent under acid-base equilibrium reveals that the oxidation of glyoxylates (Steps 2,3; **Fig. 6**) is suppressed by glyoxylate.H_2O protonation, specifically by decreasing rates of •OH-mediated glyoxylate.H_2O oxidation (Steps 3; **Fig. 6**).

The ability to mitigate inhibition of glyoxal.$2H_2O$-•OH reactions by protonating glyoxylate.H_2O (Step AB-1; **Fig. 6**) suggests that more selective •OH attack of glyoxal.$2H_2O$ would be achieved under acidic conditions. The kinetic model was used to explore such consequences of pH on glyoxal consumption rates and product distributions. The analysis was limited to 580 kHz, which achieved faster and more selective formation of C_2 acid products (**Fig. 2b,c**). **Figure 10a,c,e** shows the concentrations of glyoxal (in aldehyde and hydrated forms; a), glyoxylates (c), and oxalates (e) from the kinetic model (**Section 4.2.1**) as contour plots at fixed pH values between 0 and 5 and at different reaction times. **Figures 10b,d,f** also show contour plots for rates of glyoxal consumption (b) and of the oxidations of glyoxylates (d) and oxalates (f) by •OH. Glyoxal concentrations decreased monotonically with reaction time across all pH values, dropping below 0.5 mM within progressively shorter reaction times at lower pH (**Fig. 10a**). This glyoxal consumption trend aligns with the rate of glyoxal consumption that maintained larger values ($>4 \times 10^{-7}$ M s^{-1}) for longer durations at lower pH (**Fig. 10b**).

Concentrations of glyoxylates remained below 0.8 mM at pH 3.3, but increased significantly at lower pHs peaking above 3.3 mM below pH 1 (**Fig. 10c**). The corresponding rates for H-transfer reactions with glyoxylates became slower at early reaction times ($< 10^4$ s) with lower pH (**Fig. 10d**). The decrease in rates at lower pH despite increasing glyoxylates concentration reflects the predominance of glyoxylic acid.H_2O in acid-base equilibrium at these pH levels. These trends thus show that lowering the pH to favor the less-reactive glyoxylic acid.H_2O (Step AB-1; **Fig. 6**) suppresses the glyoxylate.H_2O-•OH reaction (Step 3; **Fig. 6**), thus promoting glyoxal activation by •OH and the formation of glyoxylates.

Oxalates yields showed two peaks, the first centered on pH 3 and the second below pH 1 (**Fig. 10e**). At pH values above 2, glyoxylates are rapidly oxidized to oxalates at the initial stages of glyoxal oxidation (between 0-10^4 s; **Fig. 10d**). The rates of oxalates-•OH reactions at these same reaction times decrease with decreasing pH (from 5 to 2 pH; **Fig. 10f**), reflecting a slower rate of oxalates decomposition via C-C cleavage (Steps 4-6; **Fig. 6**). This decrease in rate occurs at lower pH levels, despite a concomitant increase in oxalates concentrations (**Fig. 10e**), because such lower pH levels favor oxalate protonation to form hydrogen oxalate (**AB-3**). Hydrogen oxalate reacts with •OH with a slower rate constant than that of oxalate (at 325 K[34]), explaining the slower rate of oxalates decomposition. A second maximum occurs at lower pH values (below pH 1) and later reaction times (after 2×10^4 s; **Fig. 10e**). Furthermore, the consumption rates for these oxalates decrease monotonically with the pH decrease. This slower rate, which enables greater oxalates accumulation, reflects the protonation of hydrogen oxalate (**AB-2**) under acid conditions (below its pKa of 1.19 at 325; **Table S3**) to form oxalic acid. This slower rate reflects the smaller rate constant for the reaction of oxalic acid with •OH (step 4; **Fig. 6**) compared with those for both of its conjugate bases[34].

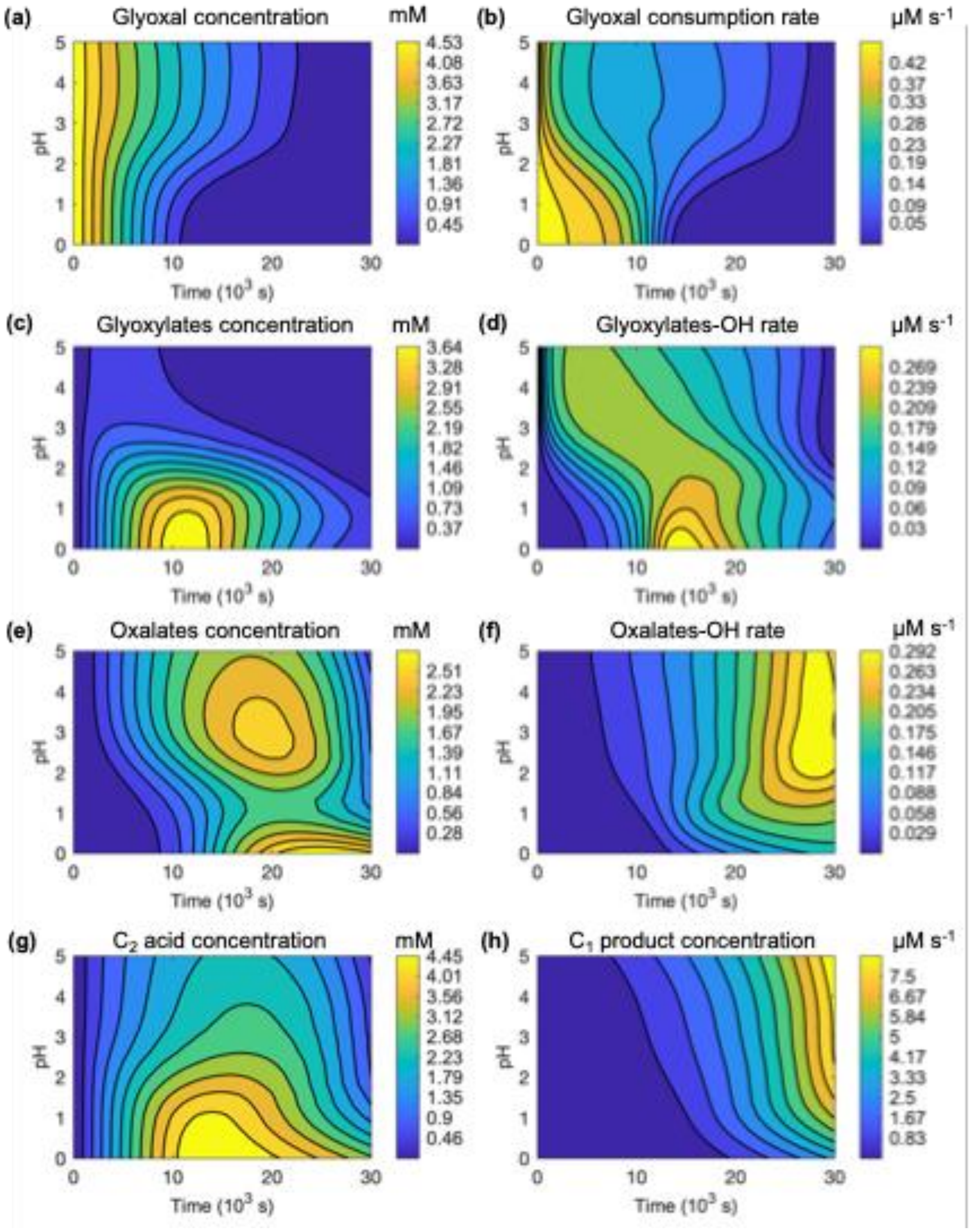

Figure 10: Contour plots for the concentrations of glyoxal (hydrated and aldehyde forms; a), glyoxylates (c), oxalates (e), C_2 acid products (glyoxylates and oxalates; g), and C_1 product (formates and carbonates; h). Rates of glyoxal consumption (b), glyoxylates consumption by reactions with •OH (d), and oxalates consumption by reactions with •OH (f). These trends are shown at different pH values and reaction times simulated with the kinetic model (Section 4.2.1) at 580 kHz of ultrasound irradiation.

The combined yields to C_2 acids (glyoxylates and oxalates) and C_1 products (formates and carbonates) at different pH levels and reaction times are shown in **Figures 10g** and **10h**. The maximum C_2 yields (for reactions at a fixed pH level) increased monotonically with decreasing pH, exceeding 4 mM, or 80% of the glyoxal reactant, at pH levels below 1 and at around 10^4 s of reaction (**Fig. 10g**). Yields of C_1 products, on the other hand, decreased monotonically with decreasing pH values, and were negligible at reaction times that maximized C_2 acids (**Fig. 10h**). The maximum yields to C_2 acids, normalized by the initial glyoxal concentration, were determined at pH values between 0 and 5, as shown in **Figure 11**. **Figure 11** also shows normalized yields of the various C_2 components (glyoxylic acid and glyoxylate in hydrated and aldehyde forms, and oxalates), the normalized yields of C_1 products, and the fractions of unreacted glyoxal at the reaction times that maximized C_2 acid yields. These normalized C_2 acid yields show a monotonic decrease with increasing pH, ranging from 0.47 to 0.97, with the highest yields obtained at the lowest pH. Glyoxylic acid yields were larger at lower pH (peaking at 0.7) and decreased asymptotically at higher pH. The glyoxylate yields were held below 0.05 across the entire pH range. The oxalates yields peaked above 0.5 at pH 3. C_1 product yields increased monotonically with increasing pH.

The influence of pH on the mechanisms of glyoxal oxidation underpins these trends in C_2 acid and C_1 product yields. Firstly, low pH favors glyoxylic acid over glyoxylate in acid-base equilibrium (Step AB-1**; Fig. 6**), which in turn (i) suppresses C-C cleavage of glyoxylate by H_2O_2 (Step 7; **Fig. 6**), and (ii) reduces •OH scavenging by glyoxylate.H_2O (Step 3; **Fig. 6**), thereby enhancing the glyoxylic acid.H_2O formation rates (via glyoxal oxidation; Step 1; **Fig. 6**). Secondly, glyoxylates accumulate substantially (**Fig. 10c**) before they are oxidized to oxalates (**Fig. 10d**), thereby delaying oxalates formation (**Fig. 10e**) and the subsequent •OH-mediated C-C cleavage (**Fig. 10**; Steps 4-6; **Fig. 6**). These findings demonstrate that controlling the kinetics of glyoxal oxidation pathways by manipulating acid-base equilibrium through changes to the pH of the solution enables the selective formation of C_2 acids even at high glyoxal conversion.

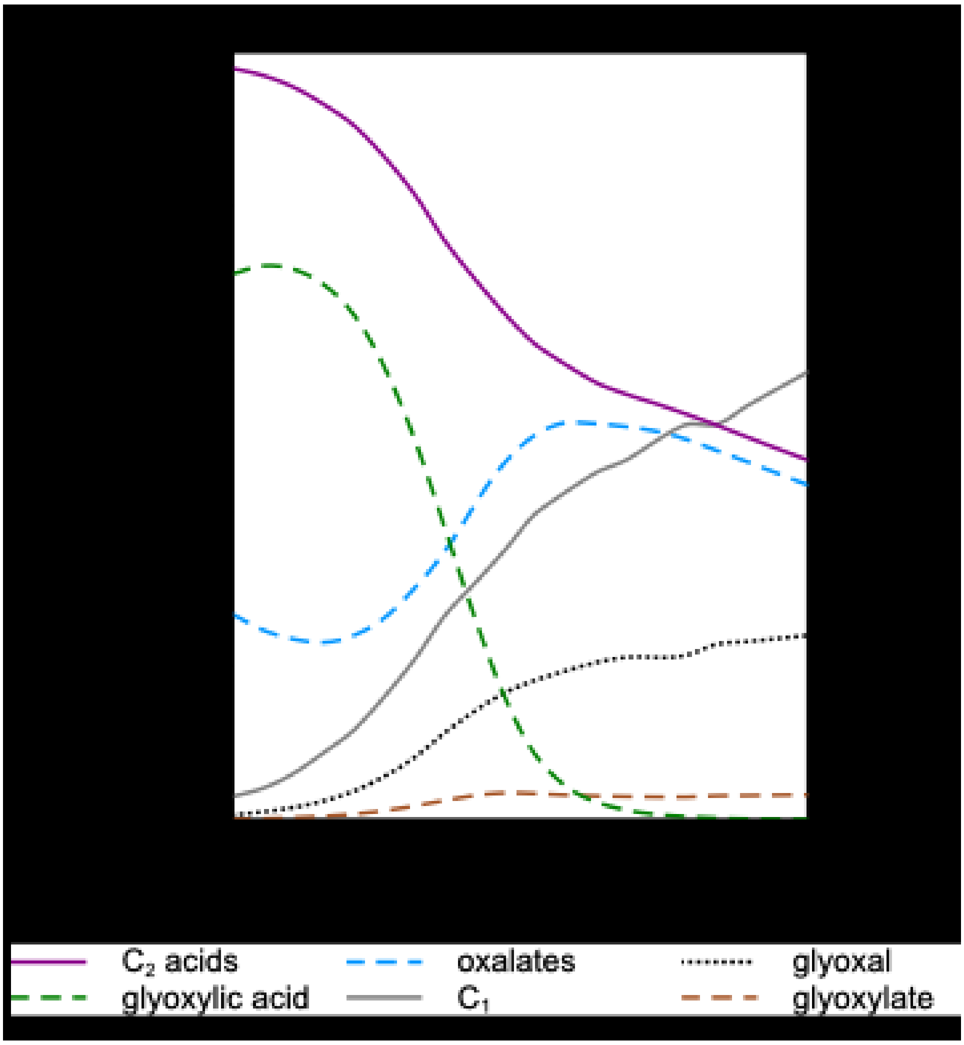

Figure 11: Maximum yields to C_2 products (glyoxylates and oxalates), and corresponding concentrations of C_1 products (formates and carbonates), glyoxylic acid, glyoxylate, oxalates and unreacted glyoxal at different pH. Yields were calculated with the kinetic model (**Section 4.2.1**) at 580 kHz and are normalized the initial glyoxal concentration (5 mM). Amounts of glyoxylic acid, glyoxylate, and glyoxal include both aldehyde and hydrated forms.

3. Conclusions

In summary, ultrasonic irradiation at 20 kHz and 580 kHz successfully oxidized aqueous glyoxal through •OH-mediated pathways into formic, glyoxylic, glycolic, and oxalic acids alongside CO_2 as primary products. Glyoxal was consumed ten-times faster at 580 kHz than at 20 kHz and with greater selectivity to C_2 acids than C_1 products. Nucleophilic $\bullet O_2^-$ addition to glyoxal monohydrate, a previously overlooked pathway, contributed significantly to rates of C-C cleavage, particularly at 20 kHz of ultrasound irradiation. Glyoxal was converted entirely at 580 kHz into these oxidation products, within experimental error. On the other hand, the majority of the glyoxal consumed at 20 kHz yielded these same oxidation products (71%), while the balance likely oligomerized through reactions between alkyl radicals and carbonyls. The •OH supply was commensurate with the amounts of glyoxal consumed at both ultrasound frequencies, thus eliminating a need to invoke aqueous pyrolysis reactions occurring at local hot spots to account for rates of glyoxal consumption.

The greater selectivity to C_2 acids at 580 kHz than at 20 kHz stemmed, in large part, from increased rates of •OH formation at 580 kHz. These increased rates promoted •OH-mediated glyoxal oxidation to C_2 acids preferentially over deleterious C-C cleavage reactions mediated by oxidation products (i.e., $•O_2^-$ and H_2O_2). Consequently, not only does the ultrasonic frequency affect the mechanical consequences of the ultrasound waves (e.g., micro-jetting, mass-transfer, shock waves) and reaction rates by introducing more radical initiators, but also the selectivity of the reactions it initiates through the interplay of reaction steps in complex reaction networks.

Rates of •OH-mediated glyoxal oxidation were suppressed through inhibition by glyoxylate and hydrogen oxalate oxidation products that scavenge •OH in electron and hydrogen-transfer reactions. Such product inhibition was mitigated under acidic conditions by protonating these carboxylates into less reactive carboxylic acids. Minimizing these secondary reactions between carboxylic acid products and •OH, moreover, was shown to avoid the C-C cleavage reactions responsible for forming C_1 products. Kinetic simulations of these reactions predicted the maximum yield to C_2 acid products possible for reactions occurring at fixed pH. Maximum yields of C_2 acids did not exceed 60% of glyoxal reactants at high pH (>3), but formed with increasing amounts at lower pH values (<2) reaching 90-97% at 0-1 pH.

Ultimately, manipulating acid-base equilibrium by controlling the pH and varying •OH formation rates by tuning the ultrasonic frequency enables ultrasound-derived •OH oxidants to selectively convert aldehyde functions into mono- or di-carboxylic acids. When powered by renewable electricity, ultrasound therefore presents a viable and sustainable strategy for selectively upgrading carbohydrate-derived platform molecules with aldehyde functions into valuable chemicals.

4. METHODS

4.1 Experimental Methods

4.1.1. Kinetic measurements for sonochemical glyoxal oxidation and H_2O_2 formation.

The oxidation of glyoxal solutions was performed at 20 kHz or 580 kHz ultrasound frequency. Reactions were performed with 100 mL of 5 mM glyoxal (prepared from 40% wt. glyoxal in H_2O; Sigma-Aldrich; distilled H_2O) at 20 kHz ultrasound in a 250 mL glass reactor with waves generated using a Digital SonifierS-250D from Branson (power of standby, P_o = 27.0 W; nominal electric power of the generator, P_{elec} = 93 W) operating at 50% wave amplitude. The waves were delivered continuously by a 13 mm diameter probe immersed directly in the reaction medium. Reactions of 5 mM glyoxal solutions (100 mL) were also performed at 580 kHz in a 250 mL glass ultrasound reactor (Meinhardt Ultrasonics Multifrequency Ultrasound reactor with a functional generator; standby power P_0 = 48 W, nominal electric power of the generator P_{elec} = 178 W) with waves delivered at 100% amplitude. The solutions in both reactors were bubbled with O_2 (Air Liquid Co) at 0.33 cm^3 s^{-1}. A Minichiller cooler (Huber) was used to dissipate the heat generated. The solutions reached steady-state temperatures of 315 K and 325 K at 20 kHz and 580 kHz, respectively.

Glyoxal, oxalic acid, glyoxylic acid, glycolic acid, and formic acid were detected and quantified using high-performance liquid chromatography (HPLC) analysis (Shimadzu HPLC; ICE-COREGEL 107H column 300 × 7.8 mm (Transgenomic)) with a UV/vis detector (Varian Pro Star, 210 nm/200 nm), a refractive index detector from Waters, pump system (LC-20AD), an autosampler SIL-10A, and CBM 20A controller. A 10 mM aqueous H_2SO_4 solution (prepared from ≥ 95% H_2SO_4 (Sigma-Aldrich) with distilled H_2O) was used as the eluent with 0.013 mL s^{-1} flow rate and oven temperature of 308 K. External calibration of liquid chromatography was performed using oxalic acid (≥99%; Sigma-Aldrich), glycolic acid (99%; Sigma-Aldrich), glyoxylic acid (98%; Sigma-Aldrich) and formic acid (98%; Acros Organics) as standards to quantify product concentrations. The complete oxidation of glyoxal to CO_2 was indirectly detected by passing the gases evolved during the reaction through a lime solution. This lime solution turned milky indicating the formation of CO_2 during glyoxal oxidation. Noteworthy, the quantification of CO_2 was not performed as it was out of the scope of this current study.

The concentrations of H_2O_2 following ultrasound irradiation of distilled H_2O (100 mL; without a substrate) in the 20 kHz and 580 kHz reactors were determined by H_2O_2 titration with Ti^{4+}.[63] An aqueous solution of $TiOSO_4$ (0.02 M) in H_2SO_4 (0.5 M; distilled H_2O) was added to samples drawn from sonication products to form a yellow-orange complex Ti(IV)-H_2O_2 [63]. The Ti(IV)-H_2O_2 absorbance was measured at 412 nm using a UV visible spectrophotometer (ThermoFisher Evolution 60S). H_2O_2 concentrations were quantified by comparison with the absorbance of standard aqueous H_2O_2 and $TiOSO_4$ solutions.

4.1.2. Detecting free radicals with electron paramagnetic resonance spectroscopy.

X-band electron paramagnetic resonance (EPR) spectroscopy (Bruker EPR A-300 spectrometer) was used to detect free radicals generated by exposing aqueous solutions of glyoxal (40 wt. % in H_2O; Shanghai Aladdin Biochemical Technological Co., Ltd) and 5,5-Dimethyl-1-pyrroline N-oxide (DMPO; Shanghai Aladdin Biochemical Technological Co., Ltd.) to ultrasonic irradiation. 15 mL solutions of 0-50 mM glyoxal and 50 mM DMPO were prepared in deionized water (18 MΩ cm^{-1}). The solutions were bubbled continuously with Ar or O_2 bubbling 0.33 cm^3 s^{-1}. The aerated solutions were then exposed to ultrasound irradiation at 20 kHz pulsed ultrasound (3 s on and 1 s off) with 25% amplitude (JY88-IIN ultrasonic processer, Shanghai Feitong Instrument Co., Ltd.; 250 W) for 1.2×10^3 s. The ultrasound waves were generated using a probe with 6 mm diameter (at the tip; Shanghai Feitong Instrument Co., Ltd.). The sonicated solutions were sampled using a quartz flat cell. The EPR spectra were collected with a 9.85 G microwave frequency, 100 G sweep width, 3505 G center field, 40 s sweep time, 2G modulation amplitude and 100 kHz modulation frequency, 20 mW microwave bridge power, 10.24 ms time constant and 20 ms conversion time. MATLAB Software (version R2022a) and EasySpin package (version 5.2.33) were used to fit observed EPR spectra to combinations of spectra of individual DMPO spin adducts.

4.2. Computational Methods

4.2.1. Calculating rate constants and constructing a kinetic model for sonochemical glyoxal oxidation.

Time-dependent reactant and product concentrations for ultrasound-driven glyoxal oxidation were simulated using a well-mixed isothermal batch reactor model. The well-mixed assumption presumes that local concentrations of chemical species do not depend significantly on the location in the reactor relative to the ultrasound source or on the proximity to nearby cavitation bubbles. Such a batch reactor model was employed successfully to study the kinetics of sonochemical oxidation of aqueous H_2S.[64] This approach differs notably from those that look explicitly at gradients in chemical potentials of radical initiators and solutes at dynamic gas-liquid interfaces[65,66].

The formation rate for each species (denoted as A with concentration $[A]$) in solution ($\partial[A]/\partial t$) was expressed by adding its formation rate from each of the N elementary steps in the proposed reaction mechanism (considering forward and reverse reactions separately), along with its volumetric generation from cavitation processes ($\dot{n}_A$):

$$\frac{\partial[A]}{\partial t} = \sum_{i}^{N} \epsilon_{Ai} r_i + \dot{n}_A \tag{4}$$

Here, r_i is the unidirectional rate for each of N elementary reactions and ϵ_{Ai} is a vector that represents the stoichiometric coefficient of A in that step. $\dot{n}_A$ was used to introduce a source of •OH to initiate homogeneous reactions ($\dot{n}_{OH}$; when A is •OH in **Eq. 4**). The value of $\dot{n}_A$ reflects a net molar rate of transport from a population of cavitation bubbles into solution within a control region, normalized by the region's volume. The $\dot{n}_{OH}$ term was assumed to be insensitive to sonication time, reflecting a steady supply of •OH, because rates of •OH formation quantified using H_2O_2 titration were constant with time (**Fig. 1**). **Equation 4** is independent of spatial dimensions, and thus implicitly assumes a sufficiently large volume element to average spatial inhomogeneities. The rate of each reaction step is proportional to a kinetic rate constant (k_i) and the concentrations of each species in solution raised to the stoichiometric coefficient (v_{iA}) for that reaction step:

$$r_i = k_i \prod_{A}^{M} [A]^{v_{iA}} \tag{5}$$

O_2, which was continuously bubbled through solution during reaction, was assumed to dissolve in solution in its equilibrium extent, dictated by Henry's law (0.99 mM kg^{-1} bar^{-1} at 20 kHz (315 K) and 0.86 mM kg^{-1} bar^{-1} at 580 kHz (325 K)[67]). The chemical activity of H_2O was maintained at unity irrespective of reaction extent.

Acids were assumed to deprotonate in equilibrium with their conjugate bases due to the rapid nature of proton transfer in H_2O[53]. Equilibrium constants (K_A) were obtained from experimental references at reaction temperatures from temperature-dependent data where available or by extrapolating from 298 K (**Table S3**). Equilibrium was established by including forward and reverse reactions for acid deprotonation as elementary steps in the reactor model. The rate constant for proton transfer from H_3O^+ to OH^- was assigned to reported values.[53] The rate constants for proton transfer from H_3O^+ to other anions, on the other hand, were assigned (**Table S3**) so as to maintain an approach to equilibrium value ($\eta = r_r/r_f$; where r_f and r_r are forward and reverse reaction rates) above 0.99 for all reactions beyond 0.5% glyoxal conversion (0.025 mM; **Section S7**), while avoiding spurious results incurred from the stiffness of the equations with larger rate constants.

Transition-state theory (TST) was used to calculate rate constants for all reactions for which a transition state (TS) could be identified using density-functional theory (DFT) based TS-search algorithms (discussed in **Section 4.2.2**). TST stipulates that rate constants (k_{TST}) depend exponentially on the free-energy barrier ($\Delta G^{\ddagger}$) associated with forming a TS from an active complex that immediately proceeds the TS along a reaction coordinate[68,69]:

$$k_{TST} = \frac{k_B T}{h} \exp\left(-\frac{\Delta G^{\ddagger}}{RT}\right) \tag{6}$$

Here, k_B is Boltzmann's constant, T is the absolute temperature, h is Plank's constant, and R is the ideal gas constant. The $\Delta G^{\ddagger}$ value was evaluated from the difference between free energy of the TS ($G^{\ddagger}$) and the active complex ($G_{A.C.}$):

$$\Delta G^{\ddagger} = G^{\ddagger} - G_{A.C.} \tag{7}$$

The free energy values were determined using the density functional theory (DFT) and statistical thermodynamics methods described in **Section 4.2.2**.

The influence of quantum tunneling on rate constants was assessed by treating barriers as parabolic and approximating a tunneling correction (κ_{QM}) using the model from Wigner[70,71]:

$$\kappa_{QM} = \frac{\alpha_0/2}{\sin(\alpha_0/2)} \tag{8}$$

Here, α_0 is defined as $\hbar\omega_{\ddagger}/k_BT$, where $\hbar$ is the reduced Plank's constant and $\omega_{\ddagger}$ is the imaginary frequency at the transition state. This expression for κ_{QM} in **Equation 8** is applicable here because α_0 values for all transition states reported are less than 2π (**Table S6**).[70] The values of κ_{QM} for all DFT-derived transition states are shown in **Table S6** alongside their corresponding imaginary frequencies. These κ_{QM} were no larger than 1.09, indicating that tunneling corrections are minor and are not needed to reach the conclusions drawn in this paper.

Rate constants for bimolecular reactions that occur without appreciable kinetic barriers, such as radical coupling reactions[72], were calculated from rates of diffusive encounters between co-reactants (denoted A and B)[73]. Rate constants for such diffusive encounters were described using formalisms developed by Smoluchowski[74]:

$$k_D = \frac{2k_BT}{3\eta}\frac{(R_{\boldsymbol{A}} + R_{\boldsymbol{B}})^2}{R_{\boldsymbol{A}}R_{\boldsymbol{B}}} \tag{9}$$

Here, η is the viscosity of water (6.29×10^{-4} at 20 kHz (315 K) and 5.29×10^{-4} at 580 kHz (325 K)[67]), and R_A and R_B are the respective molecular radii of A and B. These rate constants were of order 1.1×10^{10} M^{-1} s^{-1} at 20 kHz (315 K) and 1.4×10^{10} M^{-1} s^{-1} at 580 kHz (325 K), respectively. Their values are equivalent to those from TST (**Eq. 6**) for a hypothetical reaction with a free energy barrier of 16-20 kJ mol^{-1}. The k_D values for all steps at 315 K and 325 K are reported in the **code and data repository**. The k_D values of steps in the diffusion limit are shown in **Table S2**.

Equation 9 is derived assuming diffusion of quasi-spherical particles; therefore, the radii of spheres with equivalent volume to the molecular volume (V_M) were used to obtain $R_{\boldsymbol{A}}$ and $R_{\boldsymbol{B}}$:

$$R = \left(\frac{3V_M}{4\pi}\right)^{\frac{1}{3}} \tag{10}$$

Molecular volumes[75,76] were calculated using an algorithm herein developed that encloses the atomic coordinates of converged structures within a rectangular volume partitioned into cubes with 0.01 Å dimension. The volume is populated with van der Waals spheres[75] centered at the atomic coordinates of each constitutive atom. The molecular volume is then obtained by adding the volumes of cubes enclosed within the superimposed van der Waals spheres without double-counting. The molecular volumes and the code are reported in the **code and data repository**.

Some of the intrinsic rate constants determined from TST (k_{TST}) were of similar magnitude to diffusive rate constants (k_D). Effective rate constants (k) that reflect contributions from both intrinsic kinetics and diffusion were calculated from their resistances (k_{TST}^{-1} and k_D^{-1}, respectively) with[73]:

$$\frac{1}{k} = \frac{1}{k_{TST}} + \frac{1}{k_D} \tag{11}$$

These effective rate constants were used in kinetic models instead of k_{TST}. Their values at 298 K are reported in **Table S2**, and at 315 K and 325 K are reported in the **code and data repository**. The effective rate constants calculated using **Equation 11** differed from values reported from experiments for a set of 9 H-transfer reactions by factors ranging from 0.4-30. The ratio between experimentally measured and calculated rate constants (k_{Exp} amd k_{DFT}, respectively) were related to a difference between an effective free energy barrier corresponding to each rate constant:

$$\Delta\Delta G_{DFT}^{\ddagger} = RT \log\left(\frac{k_{Exp}}{k_{DFT}}\right) \tag{12}$$

$$\Delta\Delta G_{DFT}^{\ddagger} = \Delta G_{DFT}^{\ddagger} - \Delta G_{Exp}^{\ddagger} \tag{13}$$

Here, $\Delta G_{DFT}^{\ddagger}$ and $\Delta G_{Exp}^{\ddagger}$ are the effective free energy barriers for the rate constants. The average magnitude of $\Delta\Delta G_{DFT}^{\ddagger}$ values calculated for these same 9 H-transfer reactions was 3.6 ± 2.7 kJ mol^{-1}.

This $\Delta\Delta G^{\ddagger}_{DFT}$ falls within the error generally considered to reflect "chemical accuracy" (4 kJ mol^{-1})[38,39]. Such small differences between experimental and calculated values indicates that these methods are robust for testing mechanistic hypotheses and determining rate constants for steps in proposed reaction pathways.

Several elementary steps in the proposed mechanisms involve single-electron transfer, such as the electron transfer from the carboxylate group of oxalate to •OH. The TS of such reactions involve the migration of electrons, not nuclei, and thus could not be described with the DFT methods employed here (**Section S4**) which employ the Born-Oppenheimer approximation. Methods to treat such processes that go beyond qualitative agreement with experiments (i.e., using constrained DFT methods[77–79]) are still under active development[80]. Rate constants from experimental studies reported at sonochemical reaction temperatures, where available, or at 298 K were used instead. Their values at 298 K are shown in **Table S2** and at 315 K and 325 K in the **code and data repository**. The error introduced by using rate constants reported at 298 K without temperature corrections is not expected to influence the conclusions reached here because the values of any kinetic parameters most consequential in determining kinetic behaviours were regressed to the experimental data (see below).

Time-dependent concentrations of glyoxal and oxidation products were obtained by numerically integrating the set of ordinary differential equations represented by **Equations 4** and **5** at a certain O_2 concentration, temperature (315 K at 20 kHz and 325 K at 580 kHz), pH (**Figures 9** and **10**), and initial glyoxal concentration (5 mM). Values of $\dot{n}_{OH}$ and rate constants for two reaction steps at each frequency (with forward and reverse rate constants co-varied) were regressed to minimize the sum of the squares of the residuals between measured (**Section 4.1.1**) and predicted yields to formic, glyoxylic, and oxalic acid products using a nonlinear least-squares method (as implemented in MATLAB). Residuals for concentrations of unreacted glyoxal were not included in the regression because yields to quantified products did not close the mass balance in experiments at 20 kHz. The regressed rate constants included those for the glyoxal.2H_2O-•OH reaction (Step 7a; **Fig. S2**; k_{7a}) at both 20 kHz and 580 kHz, 2,2-dihydroxyethoxide peroxyl• protonation by H_2O (Step 11a; **Fig. S2**; k_{11a}), and the glyoxylate-H_2O_2 reaction (Step 14; **Fig. S2**; k_{14}) at 580 kHz. Here, the ".$n$$H_2O$" denotes a hydrated form of an aldehyde with *n* number of added H_2O molecules. Values of k_{7a} where regressed because a sensitivity analysis based on degree of rate control formalisms[61,62] showed their values contributed most significantly to the model error (**Section S8**). Regressing k_{11a} and k_{14} at 20 kHz and 580 kHz, respectively, was required to produce the measured formic acid yields in both magnitude and curvature (**Section S8**).

4.2.2. Density functional theory and statistical methods for determining thermochemistry and kinetic barriers.

Density functional theory methods (as implemented in QChem 5.4.1)[81] were used to calculate molecular geometries and energetic properties of species participating in proposed reaction networks. Molecular structures were converged to their minimum potential of mean force (PMF; with wavefunction error less than 10^{-7} Ha) using the ωB97M-V functional[37] and 6-311++G(2df,2p) basis set with the SMD implicit solvation model[36]. Unrestricted orbitals were used to converge structures with unpaired electrons including (i) radicals with odd numbers of electrons (e.g. •OH) and a spin multiplicity of two and (ii) diradical molecules with even numbers of electrons (i.e. triplet O_2) with a spin multiplicity of three. Harmonic vibrational frequencies at stationary points corresponding to reactant, transition, and product states for each elementary step were evaluated from the eigenvalues of the Hessian matrix (with a finite differences step of 0.001 a.u). The vibrational frequencies were obtained from minima on the PMF surface and computed in the presence of the SMD model, as recommended elsewhere[82].

The TS for elementary reaction steps (stationary states with a single negative eigenvalue of the Hessian matrix) were located using the partitioned rational function optimization (P-RFO) algorithm from Baker[83]. The energy and gradient convergence criteria of $<10^{-6}$ Ha and $<3\times10^{-4}$ Ha, respectively were employed. The Hessian matrix of the resulting TS was evaluated with a finite differences step of 0.001 a.u to ensure a single negative eigenvalue for each TS structure and confirm their location at a saddle point on the PMF surface. These imaginary frequencies are reported in **Table S6**. The initial guesses for TS geometries for the P-RFO calculation were determined either by (i) manually manipulating the reactant state geometry or (ii) using the freezing string method[84]. The intrinsic reaction coordinate (IRC) analysis[85] was used to confirm that the TS connects the intended reactants and products along the reaction coordinate. The IRC analysis failed in a few instances (**Table S6**); the imaginary modes of these structures were inspected to ensure motion along the expected reaction coordinate. Barriers calculated with the 6-311++G(2df,2p) basis set converged within 1 kJ mol^{-1} of those calculated with the larger 6-311++G(3df,2p) basis set for five model reactions (**Section S9**). These barriers differed with mean absolute errors of 1.6 ± 1.0 kJ mol^{-1} of those calculated using the largest basis set (def2-QZVP). Such convergence indicates that the mechanistic conclusions drawn from kinetic parameters calculated with these barriers are not sensitive to the choice of the type of basis set used or its size.

The free energies of solutes at stationary points under reaction conditions (G_s) were calculated from DFT-based methods and statistical thermodynamics formalisms established previously[82,86]. DFT calculations in QChem using the SMD solvation model were used to calculate a free energy (denoted as $G°_S$; with standard state of 1 M at 298 K) of the solute which averages over all solvent, but not solute, degrees of freedom[36]. It includes the influence of solute-solvent electronic interactions, polarization, solvent cavity formation, dispersion energy, and changes to the local solvent structure on the solute's free energy[36]. These $G°_S$ values are calculated at 298 K and were used to describe solute free energies at reaction temperatures (315 K and 325 K) without applying temperature corrections. The free energy of the solute averaging over all solute degrees of freedom was obtained from the $G°_S$ values by accounting for additional contributions from zero-point energy (ZPE), liberational free energy (G_{lib}), rotational-vibrational free energy (G_{ro-vib}), and electronic entropy (S_{elec}):

$$G_s = G°_S + ZPE + G_{lib} + G_{ro-vib} - TS_{elec} \tag{14}$$

The G_s reported here considered only a single conformer without conformational free energy. These G_s values were used to determine free energies of intermediates and TSs for calculating equilibrium and rate coefficients in the reaction mechanism. An implementation of these thermochemical calculations is available in the **code and data repository**.

The zero-point energy (ZPE) was obtained from DFT-derived vibrational modes calculated on the PMF surface (Section 2.2) using the harmonic oscillator approximation. The S_{elec} value was determined from the spin multiplicity using standard methods[87].

The liberational free energy of a solute in solution is equivalent to the translational free energy of the solute at the same concentration as an ideal gas[82,86]. G_{lib} was therefore calculated using the translational enthalpy (H_{trans}) and entropy (S_{trans}) of an ideal gas ($G_{lib} = H_{trans} - TS_{trans}$) following standard statistical thermodynamics formalisms evaluated at reaction temperature[87], ensuring a standard state of 1 M at 298 K.

The G_{ro-vib} term was approximated by separating its value into rotational free energy (G_{rot}) and vibrational free energy (G_{vib}) components. G_{rot} is calculated from the solute partition function for unhindered rotations[87] (at reaction temperatures), which has been suggested to be a useful approximation of the free energy of librations in solution[82]. The principle moments of inertia used to calculate G_{rot} were obtained from QChem. G_{vib} was calculated from the solute vibrational partition function in the harmonic oscillator approximation[87] (at reaction temperatures) with vibrational frequencies calculated using the SMD solvation model from PMF minima. In calculating vibrational entropy, vibrational modes below 100 cm^{-1} were replaced with 100 cm^{-1} to avoid well-established numerical artifacts[82],[88].

ASSOCIATED CONTENT

Supporting Information

All Supporting Information is available free of charge on the ChemSusChem webpage. These include supplemental EPR results, a comprehensive reaction mechanism, calculated kinetic and thermodynamic coefficients, kinetic model validation, supplemental kinetic analysis and discussion, a basis set convergence test, supplemental analysis of transition state calculations, and additional references. These materials are contained within Sections S1-S11, Figures S1-S14, Tables S1-S6, Equations S1-S4, and the Supplemental References section.

Data Availability Statement

The datasets and original codes generated during this study are publicly available: https://github.com/ari-fischer/glyoxal_oxidation_2024.git. These datasets and original codes include: DFT output files for stationary points needed to generate kinetic and thermodynamic parameters, for the basis set convergence test, and for and additional calculations reported; the Jupyter notebook and dependences to generate the input files for microkinetic model implemented in MATLAB and outputs at LFUS (20 kHz) and HFUS (580 kHz); the microkinetic model implemented in MATLAB for generating reaction rates and trends; the kinetic and thermodynamic coefficients evaluated at 315 K and 325 K and inputs to MKM model; and the python code for calculating van der Waals volumes.

AUTHOR INFORMATION

Corresponding Authors

*Wen Liu (wenliu@ntu.edu.sg), Prince N. Amaniampong (prince.nana.amaniampong@univ-poitiers.fr), and Tej S. Choksi (tej.choksi@ntu.edu.sg)

Notes

The authors declare no competing financial interests

Author Contributions

Conceptualization: AF and TC conceptualized the mechanistic description, kinetic modeling approach, explanations for the effects of ultrasound frequency on selectivity, and the selectivity control. *Data curation:* AF constructed the code and data repository. *Formal analysis:* AF performed the DFT calculations and the kinetic analyses; TB obtained yields from experimental kinetic data; ZX analyzed EPR spectra. *Funding acquisition:* PA, TC, and WL acquired financial support for the study. *Investigation:* TB performed kinetic measurements. ZX performed EPR measurements. *Methodology:* AF and TC designed the methodologies of kinetic analyses. AF constructed the kinetic models. PA and TB designed and conducted the sonochemical kinetic experiments. KQ, RL, WL, and ZX designed the methodology for EPR experiments. *Project administration:* PA, TC, and WL managed and coordinated the research activities. *Resources:* TC provided computational resources. FJ and PA provided experimental resources for the kinetic measurements. RL and WL provided experimental resources for EPR measurements. *Software:* AF developed all new codes and algorithms used in the computational studies and implemented QChem software for the investigation. *Supervision:* TC supervised the computational research. FJ and PA supervised the kinetic experiments. RL and WL supervised the EPR measurements. *Visualization:* ZX created the figures for the EPR studies. AF created all other figures and illustrations. *Writing-original draft:* AF and TC drafted the main text of the original manuscript, modeling sections of the methods, supporting information, and data repository. AF, TB, and ZX drafted the experimental methods. *Writing-review & editing:* All authors reviewed and edited the manuscript.

ACKNOWLEDGEMENTS

This project was funded by the National Research Foundation (NRF), Prime Minister's Office, Singapore under its Campus for Research Excellence and Technological Enterprise (CREATE) programme and the Ministry of Research Academic Research Fund Tier-1: RG87/23. This project was also supported by the NRF-ANR Joint Research Project (NRF2020-NRF-ANR066 SonoNanoCat) jointly funded by NRF and the French National Research Agency (ANR). Additional funding came from the Engineering and Physical Sciences Research Council of the UK (Grant number EP/W012316/1). Dr. Teseer Bahry, Dr. François Jérôme, Dr. Sabine Valange and Dr. Prince N. Amaniampong acknowledge financial support from the European Union (ERDF) and Région Nouvelle Aquitaine. We acknowledge the High-Performance Computing (HPC) team at the HPC Centre, NTU for technical assistance and computing resources. The authors acknowledge Dr. Luan Q. Le for discussions about the mechanism and kinetic modeling, Dr. Robert Batista da Silva Junior for experimental findings that helped inspire these studies, and Dr. Shaama M. Sharada for insights into the DFT methods used.

REFERENCES

[1] W. Deng, Q. Zhang, Y. Wang, *Catalysis Today* **2014**, *234*, 31–41.
[2] G. M. Rodriguez, S. Atsumi, *Microb Cell Fact* **2012**, *11*, 90–101.
[3] Y. Doleyres, P. Beck, S. Vollenweider, C. Lacroix, *Appl Microbiol Biotechnol* **2005**, *68*, 467–474.

[4] E. V. Makshina, J. Canadell, J. van Krieken, E. Peeters, M. Dusselier, B. F. Sels, *ChemCatChem* **2019**, *11*, 180–201.
[5] K. Shimizu, A. Satsuma, *Energy Environ. Sci.* **2011**, *4*, 3140–3153.
[6] J. J. Bozell, G. R. Petersen, *Green Chem.* **2010**, *12*, 539.
[7] Y. B. Lim, Y. Tan, M. J. Perri, S. P. Seitzinger, B. J. Turpin, *Atmospheric Chemistry and Physics* **2010**, *10*, 10521–10539.
[8] Y. Tan, M. J. Perri, S. P. Seitzinger, B. J. Turpin, *Environ. Sci. Technol.* **2009**, *43*, 8105–8112.
[9] B. Ervens, R. Volkamer, *Atmos. Chem. Phys.* **2010**, *10*, 8219–8244.
[10] Y. B. Lim, Y. Tan, B. J. Turpin, *Atmos. Chem. Phys.* **2013**, *13*, 8651–8667.
[11] Y. Tan, Y. B. Lim, K. E. Altieri, S. P. Seitzinger, B. J. Turpin, *Atmos. Chem. Phys.* **2012**, *12*, 801–813.
[12] Y. Tan, A. G. Carlton, S. P. Seitzinger, B. J. Turpin, *Atmospheric Environment* **2010**, *44*, 5218–5226.
[13] M. J. Perri, S. Seitzinger, B. J. Turpin, *Atmospheric Environment* **2009**, *43*, 1487–1497.
[14] D. Ma, H. Yi, C. Lai, X. Liu, X. Huo, Z. An, L. Li, Y. Fu, B. Li, M. Zhang, L. Qin, S. Liu, L. Yang, *Chemosphere* **2021**, *275*, 130104.
[15] L. Schöne, H. Herrmann, *Atmos. Chem. Phys.* **2014**, *14*, 4503–4514.
[16] J. Kim, C.-H. Huang, *ACS EST Water* **2021**, *1*, 15–33.
[17] G. V. Buxton, C. L. Greenstock, W. P. Helman, A. B. Ross, *Journal of Physical and Chemical Reference Data* **1988**, *17*, 513–886.
[18] K. Makino, M. M. Mossoba, P. Riesz, *J. Phys. Chem.* **1983**, *87*, 1369–1377.
[19] M. R. Hoffmann, I. Hua, R. Höchemer, *Ultrasonics Sonochemistry* **1996**, *3*, S163–S172.
[20] E. B. Flint, K. S. Suslick, *Science* **1991**, *253*, 1397–1399.
[21] K. S. Suslick, *Science* **1990**, *247*, 1439–1445.
[22] P. R. Gogate, A. B. Pandit, *Ultrasonics Sonochemistry* **2004**, *11*, 105–117.
[23] B. D. Storey, A. J. Szeri, *Proc. R. Soc. Lond. A* **2000**, *456*, 1685–1709.
[24] A. Kotronarou, G. Mills, M. R. Hoffmann, *Environ. Sci. Technol.* **1992**, *26*, 2420–2428.
[25] A. Kotronarou, G. Mills, M. R. Hoffmann, *J. Phys. Chem.* **1991**, *95*, 3630–3638.
[26] T. Kondo, C. M. Krishna, P. Riesz, *Radiation Research* **1989**, *118*, 211.
[27] G. Chatel, J. C. Colmenares, *Top Curr Chem (Z)* **2017**, *375*, 8, s41061-016-0096–1.
[28] M. Draye, N. Kardos, *Top Curr Chem (Z)* **2016**, *374*, 74.
[29] H. Heusinger, *Ultrasonics* **1990**, *28*, 30–36.
[30] H. Heusinger, *Carbohydrate Research* **1988**, *181*, 67–75.
[31] K. S. Suslick, D. A. Hammerton, R. E. Cline, *J. Am. Chem. Soc.* **1986**, *108*, 5641–5642.
[32] B. D. Storey, A. J. Szeri, *Proc. R. Soc. Lond. A* **2001**, *457*, 1685–1700.
[33] E. J. Hart, A. Henglein, *J. Phys. Chem.* **1985**, *89*, 4342–4347.
[34] B. Ervens, S. Gligorovski, H. Herrmann, *Phys. Chem. Chem. Phys.* **2003**, *5*, 1811–1824.
[35] R. Huie, **2003**.
[36] A. V. Marenich, C. J. Cramer, D. G. Truhlar, *J. Phys. Chem. B* **2009**, *113*, 6378–6396.
[37] N. Mardirossian, M. Head-Gordon, *The Journal of Chemical Physics* **2016**, *144*, 214110.
[38] M. Bursch, J. Mewes, A. Hansen, S. Grimme, *Angew Chem Int Ed* **2022**, *61*, e202205735.
[39] A. Galano, J. R. Alvarez- Idaboy, *J Comput Chem* **2013**, *34*, 2430–2445.
[40] W. H. Green, *Advances in Chemical Engineering* **2007**, *32*, 1–50.
[41] B. Wei, R. Zhang, P. H.-L. Sit, M. He, C. K. Chan, *Environ. Sci.: Atmos.* **2023**, *3*, 1296–1305.
[42] H. S. S. Ip, X. H. H. Huang, J. Z. Yu, *Geophysical Research Letters* **2009**, *36*, 2008GL036212.

[43] S. Merouani, O. Hamdaoui, Y. Rezgui, M. Guemini, *Acta Acustica united with Acustica* **2014**, *100*, 823–833.
[44] G. Mark, A. Tauber, R. Laupert, H.-P. Schuchmann, D. Schulz, A. Mues, C. Von Sonntag, *Ultrasonics Sonochemistry* **1998**, *5*, 41–52.
[45] R. F. Martínez, G. Cravotto, P. Cintas, *J. Org. Chem.* **2021**, *86*, 13833–13856.
[46] R. Pflieger, T. Chave, G. Vite, L. Jouve, S. I. Nikitenko, *Ultrasonics Sonochemistry* **2015**, *26*, 169–175.
[47] E. Dalodière, M. Virot, P. Moisy, S. I. Nikitenko, *Ultrasonics Sonochemistry* **2016**, *29*, 198–204.
[48] S. Merouani, H. Ferkous, O. Hamdaoui, Y. Rezgui, M. Guemini, *Ultrasonics Sonochemistry* **2015**, *22*, 51–58.
[49] D. Behar, G. Czapski, J. Rabani, L. M. Dorfman, H. A. Schwarz, *J. Phys. Chem.* **1970**, *74*, 3209–3213.
[50] A. R. Rendina, J. D. Hermes, W. W. Cleland, *Biochemistry* **1984**, *23*, 5148–5156.
[51] M. Hayyan, M. A. Hashim, I. M. AlNashef, *Chem. Rev.* **2016**, *116*, 3029–3085.
[52] R. P. Bell, P. T. McTigue, *J. Chem. Soc.* **1960**, 2983.
[53] F. H. Stillinger, in *Theoretical Chemistry*, Elsevier, **1978**, pp. 177–234.
[54] D. A. Weil, D. A. Dixon, *J. Am. Chem. Soc.* **1985**, *107*, 6859–6865.
[55] F. E. Wilkinson, M. Peschke, J. E. Szulejko, T. B. McMahon, *International Journal of Mass Spectrometry and Ion Processes* **1998**, *175*, 225–240.
[56] T. Mill, D. G. Hendry, *Comprehensive Chemical Kinetics* **1980**, *16*, 1–87.
[57] E. Bothe, M. N. Schuchmann, D. Schulte-Frohlinde, C. V. Sonntag, *Zeitschrift für Naturforschung B* **1983**, *38*, 212–219.
[58] G. V. Buxton, Malone, Treena N., Salmon, G. Arthur, *J. Chem. Soc., Faraday Trans.* **1997**, *93*, 2889–2891.
[59] J. J. Grabowski, C. H. DePuy, V. M. Bierbaum, *J. Am. Chem. Soc.* **1983**, *105*, 2565–2571.
[60] H. Hippler, B. Viskolcz, *Phys. Chem. Chem. Phys.* **2002**, *4*, 4663–4668.
[61] C. T. Campbell, *Top Catal* **1994**, *1*, 353–366.
[62] C. T. Campbell, *ACS Catal.* **2017**, *7*, 2770–2779.
[63] G. Schwarzenbach, J. Muehlebach, K. Mueller, *Inorg. Chem.* **1970**, *9*, 2381–2390.
[64] A. Kotronarou, M. R. Hoffmann, in *Aquatic Chemistry: Interfacial and Interspecies Processes* (Eds.: C.P. Huang, C.R. O'Melia, J.J. Morgan), American Chemical Society, Washington, DC, **1995**.
[65] K. Peng, S. Tian, Y. Zhang, Q. He, Q. Wang, *Ultrasonics Sonochemistry* **2022**, *91*, 106235.
[66] K. Peng, F. G. F. Qin, R. Jiang, W. Qu, Q. Wang, *Ultrasonics Sonochemistry* **2022**, *88*, 106067.
[67] J. A. Manion, R. E. Huie, R. D. Levin, D. R. Burgess Jr, W. L. Orkin, W. Tsang, W. S. McGivern, J. W. Hudgens, V. D. Knyazev, D. B. Atkinson, E. Chai, A. M. Tereza, C.-Y. Lin, T. C. Allison, W. G. Mallard, F. Westley, J. T. Herron, R. F. Hampson, D. H. Frizzell, "NIST Chemical Kinetics Database, NIST Standard Reference Database 17, Version 7.0 (Web Version), Release 1.6.8, Data version 2015.09, National Institute of Standards and Technology, Gaithersburg, Maryland, 20899-8320.," **2015**.
[68] H. Eyring, *The Journal of chemical physics* **1935**, *3*, 107–115.
[69] B. Peters, in *Reaction Rate Theory and Rare Events Simulations*, Elsevier, **2017**, pp. 227–271.
[70] B. Peters, in *Reaction Rate Theory and Rare Events Simulations*, Elsevier, **2017**, pp. 311–333.
[71] E. Wigner, *Phys. Rev.* **1932**, *40*, 749–759.

[72] C. H. Bamford, C. F. H. Tipper, R. G. Compton, Eds. , in *Diffusion-Limited Reactions*, Elsevier, **1985**, pp. 3–46.

[73] B. Peters, in *Reaction Rate Theory and Rare Events Simulations*, Elsevier, **2017**, pp. 129–145.

[74] M. v Smoluchowski, *Zeitschrift für Physikalische Chemie* **1918**, *92U*, 129–168.

[75] A. Bondi, *J. Phys. Chem.* **1964**, *68*, 441–451.

[76] O. J. Conquest, T. Roman, A. Marianov, A. Kochubei, Y. Jiang, C. Stampfl, *J. Chem. Theory Comput.* **2021**, *17*, 7753–7771.

[77] A. Hashemi, P. Peljo, K. Laasonen, *J. Phys. Chem. C* **2023**, *127*, 3398–3407.

[78] Q. Wu, T. Van Voorhis, *J. Chem. Theory Comput.* **2006**, *2*, 765–774.

[79] Q. Wu, T. Van Voorhis, *J. Phys. Chem. A* **2006**, *110*, 9212–9218.

[80] K. J. Kron, A. Rodriguez-Katakura, R. Elhessen, S. Mallikarjun Sharada, *ACS Omega* **2021**, *6*, 33253–33264.

[81] Y. Shao, Z. Gan, E. Epifanovsky, A. T. B. Gilbert, M. Wormit, J. Kussmann, A. W. Lange, A. Behn, J. Deng, X. Feng, D. Ghosh, M. Goldey, P. R. Horn, L. D. Jacobson, I. Kaliman, R. Z. Khaliullin, T. Kuś, A. Landau, J. Liu, E. I. Proynov, Y. M. Rhee, R. M. Richard, M. A. Rohrdanz, R. P. Steele, E. J. Sundstrom, H. L. Woodcock, P. M. Zimmerman, D. Zuev, B. Albrecht, E. Alguire, B. Austin, G. J. O. Beran, Y. A. Bernard, E. Berquist, K. Brandhorst, K. B. Bravaya, S. T. Brown, D. Casanova, C.-M. Chang, Y. Chen, S. H. Chien, K. D. Closser, D. L. Crittenden, M. Diedenhofen, R. A. DiStasio, H. Do, A. D. Dutoi, R. G. Edgar, S. Fatehi, L. Fusti-Molnar, A. Ghysels, A. Golubeva-Zadorozhnaya, J. Gomes, M. W. D. Hanson-Heine, P. H. P. Harbach, A. W. Hauser, E. G. Hohenstein, Z. C. Holden, T.-C. Jagau, H. Ji, B. Kaduk, K. Khistyaev, J. Kim, J. Kim, R. A. King, P. Klunzinger, D. Kosenkov, T. Kowalczyk, C. M. Krauter, K. U. Lao, A. D. Laurent, K. V. Lawler, S. V. Levchenko, C. Y. Lin, F. Liu, E. Livshits, R. C. Lochan, A. Luenser, P. Manohar, S. F. Manzer, S.-P. Mao, N. Mardirossian, A. V. Marenich, S. A. Maurer, N. J. Mayhall, E. Neuscamman, C. M. Oana, R. Olivares-Amaya, D. P. O’Neill, J. A. Parkhill, T. M. Perrine, R. Peverati, A. Prociuk, D. R. Rehn, E. Rosta, N. J. Russ, S. M. Sharada, S. Sharma, D. W. Small, A. Sodt, T. Stein, D. Stück, Y.-C. Su, A. J. W. Thom, T. Tsuchimochi, V. Vanovschi, L. Vogt, O. Vydrov, T. Wang, M. A. Watson, J. Wenzel, A. White, C. F. Williams, J. Yang, S. Yeganeh, S. R. Yost, Z.-Q. You, I. Y. Zhang, X. Zhang, Y. Zhao, B. R. Brooks, G. K. L. Chan, D. M. Chipman, C. J. Cramer, W. A. Goddard, M. S. Gordon, W. J. Hehre, A. Klamt, H. F. Schaefer, M. W. Schmidt, C. D. Sherrill, D. G. Truhlar, A. Warshel, X. Xu, A. Aspuru-Guzik, R. Baer, A. T. Bell, N. A. Besley, J.-D. Chai, A. Dreuw, B. D. Dunietz, T. R. Furlani, S. R. Gwaltney, C.-P. Hsu, Y. Jung, J. Kong, D. S. Lambrecht, W. Liang, C. Ochsenfeld, V. A. Rassolov, L. V. Slipchenko, J. E. Subotnik, T. Van Voorhis, J. M. Herbert, A. I. Krylov, P. M. W. Gill, M. Head-Gordon, *Molecular Physics* **2015**, *113*, 184–215.

[82] R. F. Ribeiro, A. V. Marenich, C. J. Cramer, D. G. Truhlar, *J. Phys. Chem. B* **2011**, *115*, 14556–14562.

[83] J. Baker, *J Comput Chem* **1986**, *7*, 385–395.

[84] A. Behn, P. M. Zimmerman, A. T. Bell, M. Head-Gordon, *The Journal of Chemical Physics* **2011**, *135*, 224108.

[85] K. Fukui, *J. Phys. Chem.* **1970**, *74*, 4161–4163.

[86] Y. Kim, J. R. Mohrig, D. G. Truhlar, *J. Am. Chem. Soc.* **2010**, *132*, 11071–11082.

[87] K. K. Irikura, “Thermochemistry, Essential Statistical Thermodynamics,” can be found under https://cccbdb.nist.gov/thermox.asp, **n.d.**

[88] P. Pracht, S. Grimme, *Chem. Sci.* **2021**, *12*, 6551–6568.